Available online at www.sciencedirect.com
ScienceDirect
Journal of Computational Physics 227 (2008) 7446–7468
JOURNAL OF COMPUTATIONAL PHYSICS
www.elsevier.com/locate/jcp

An implicit technique for solving 3D low Reynolds number moving free surface flows

Cassio M. Oishi [a], Murilo F. Tomé [a], José A. Cuminato [a], Sean McKee [b,*]

[a] *Departamento de Matemática, Aplicada e Estatística, Instituto de Ciências Matemáticas e de Computação, Universidade de São Paulo, São Carlos, Brazil*
[b] *Department of Mathematics, University of Strathclyde, Glasgow, UK*

Received 17 October 2007; received in revised form 10 April 2008; accepted 11 April 2008
Available online 30 April 2008

Abstract

This paper describes the development of an implicit finite difference method for solving transient three-dimensional incompressible free surface flows. To reduce the CPU time of explicit low-Reynolds number calculations, we have combined a projection method with an implicit technique for treating the pressure on the free surface. The projection method is employed to uncouple the velocity and the pressure fields, allowing each variable to be solved separately. We employ the normal stress condition on the free surface to derive an implicit technique for calculating the pressure at the free surface. Numerical results demonstrate that this modification is essential for the construction of methods that are more stable than those provided by discretizing the free surface explicitly. In addition, we show that the proposed method can be applied to viscoelastic fluids. Numerical results include the simulation of jet buckling and extrudate swell for Reynolds numbers in the range $[0.01, 0.5]$.

Keywords: Implicit techniques; Three-dimensional free surface flows; Viscoelastic fluids; Finite differences; Jet buckling; Extrudate swell

1. Introduction

A very active and important research area in Computational Fluid Dynamics is the development of computational methods for free surface flows. This can be explained by the fact that flows with free surfaces are more difficult to resolve in general than confined flows. The position of the boundary is known only at the initial time, and its new position has to be determined as part of the solution. The MAC method (Marker-and-Cell), introduced by Harlow and Welch [18], was one of the first successful attempts to simulate viscous, incompressible, transient flows with free surfaces. MAC was derived from the discretization of the Navier–Stokes equations in primitive variables by finite differences on a uniform staggered mesh. In this method, the shape of the free surface is determined by cells that are partially filled. Variants of the MAC method with

* Corresponding author. Tel.: +44 141 548 3671.
E-mail address: smck@maths.strath.ac.uk (S. McKee).

0021-9991/$ - see front matter © 2008 Elsevier Inc. All rights reserved.
doi:10.1016/j.jcp.2008.04.017

distinct versions are widely available in the literature (see e.g. [2,8,9,18,19,25,33,41], and many others). However, one feature common to almost all these techniques is the explicit time discretization of the momentum equations by Euler's method. Indeed, for inertial flows ($Re > 1$) explicit methods do not impose too severe a restriction on the time step so that numerical solutions of free surface flows can be obtained in reasonable time (e.g. [38]). However, Reynolds numbers of order 10^{-1} to 10^{-3} can be easily found in applications involving the flow of polymers such as extrudate swell, injection moulding and jet buckling. For low Reynolds number flows, explicit methods have a stringent stability restriction leading to very small time steps. One way to overcome this restriction is to use an implicit discretization that, one might expect, would lead to a substantial reduction in CPU time. There would appear to be only a few papers (e.g. [13,15,17,31,33,47]) presenting implicit formulations for free surface flows, and these tend to be for two-dimensional flows where the Reynolds number is not excessively small. However, there are some works that employ the level set method to model free surface flows. For instance, Fedkiw et al. [12] presented a numerical method for treating interfaces using an Eulerian scheme for multi-material flows while Nguyen et al. [26] solved the Euler equations to simulate multiphase flows of inviscid fluids. To calculate the velocity field they used the projection method in a similar fashion as in the MAC method [18]. They reported some results for 1D, 2D and 3D problems. One interesting work that deals with free surface viscous flows was presented by Vincent and Caltagirone [45] (see also [46]). They solved the full Navier–Stokes equations for interfacial flows on a staggered grid using the finite volume method. The interface was represented by an advection equation which was treated by a high order TVD (Total Variation Diminishing) scheme. Their results include the simulation of 3D advection of a sphere and the simulation of a 2D Newtonian jet filling a square box.

More recently, the authors presented a novel two-dimensional implicit method (see Oishi et al. [28]) for unsteady two-dimensional free surface flows using a Marker-and-Cell approach. In that method the implicit Euler scheme was employed in the discretization of the diffusion terms while the free surface boundary conditions were discretized implicitly. Numerical experiments obtained by Oishi et al. [28] suggested that when the equation for the pressure on the free surface was discretized explicitly, a parabolic-type stability condition was required to be imposed on the time step, independently of whether the diffusion terms of the Navier–Stokes equations were discretized explicitly or implicitly. Indeed, it was found numerically that in order to obtain a stable implicit solver for the Navier–Stokes equations it was crucial that the pressure condition at the free surface was required to be solved implicitly. However, when the pressure equation at the free surface was discretized implicitly it coupled the velocity and pressure fields so that a much larger linear system had to be solved at each time step. To overcome this, Oishi et al. [28] developed numerical techniques for uncoupling the velocity and pressure fields while still maintaining the implicit discretization of the pressure equation at the free surface. More recently, Oishi et al. [29] have performed a rigorous stability analysis on discretizations of a paradigm problem, the 1-D heat equation, solved on a staggered grid with the implicit boundary conditions replaced by explicit boundary conditions and this model problem has shed light as to why the approach described above is effective.

In this work we employ the ideas presented by Oishi et al. (see [28]) to develop a stable 3D implicit method for solving incompressible free surface flows. This novel formulation combines an accurate projection method (described in [30]) with a new formula for the pressure-update and an implicit technique for computing the pressure on the free surface. This last point is very important because, as was shown in [28], the implicit discretization of the boundary conditions at the free surface is crucial for achieving a stable implicit method. The performance of the numerical method is demonstrated by simulating three-dimensional free surface flow problems with low Reynolds numbers and moving free surfaces. Moreover, we show that the proposed method can also be applied to viscoelastic fluids.

This paper is organized as follows. First the governing equations together with the boundary conditions are described. Section 3 presents the details of the numerical method: a description of the projection method, the implicit formulation for the pressure at the free surface, the algorithm itself, the detailed finite difference approximations and a discussion on the time step stability restriction. Numerical results are given in Section 4. The flow of an Oldroyd-B fluid inside a 3D tube is simulated and compared with the corresponding analytic solution. A comparison between the explicit and implicit techniques is then effected. Finally, the implicit technique is employed to solve complex free surface flows: both extrudate swell of a 3D Oldroyd-B fluid and the

buckling of a Newtonian jet are simulated; extremely small Reynolds numbers were used in both cases. Section 5 contains some concluding remarks.

2. Governing equations and boundary conditions

In dimensionless conservative form, the equations for incompressible viscous flow in primitive variables can be written as

$$\frac{\partial \mathbf{u}}{\partial t} + \nabla \cdot (\mathbf{u}\mathbf{u}) = -\nabla p + \alpha \frac{1}{Re}\nabla^2 \mathbf{u} + \beta \nabla \cdot \mathbf{S} + \frac{1}{Fr^2}\mathbf{g}, \tag{1}$$

and the mass conservation equation as

$$\nabla \cdot \mathbf{u} = 0, \tag{2}$$

where $\mathbf{S}$ is the non-Newtonian part of the extra stress tensor (hereafter simply called the non-Newtonian stress tensor) that is defined by an appropriate constitutive relationship. For Newtonian flows $\mathbf{S} = \mathbf{0}$ so this can be achieved by setting $\alpha = 1$ and $\beta = 0$ in the momentum Eq. (1). In this work we shall also be concerned with viscoelastic flows governed by the Oldroyd-B constitutive equation. In this case, we set $\alpha = \frac{\lambda_2}{\lambda_1}$ and choose $\beta = 1$ in the momentum equation. The non-Newtonian stress tensor $\mathbf{S}$ is obtained from the Oldroyd-B constitutive relationship (see Tomé et al. [44])

$$\frac{\partial \mathbf{S}}{\partial t} = -(\mathbf{u}\cdot\nabla)\mathbf{S} + (\nabla \mathbf{u})^T\mathbf{S} + \mathbf{S}(\nabla \mathbf{u}) + \frac{1}{We}\left[\frac{1}{Re}\left(1 - \frac{\lambda_2}{\lambda_1}\right)((\nabla \mathbf{u}) + (\nabla \mathbf{u})^T) - \mathbf{S}\right], \tag{3}$$

where λ_1 and λ_2 are relaxation and retardation time constants, respectively, characterizing the Oldroyd-B model and $We = \lambda_1 \frac{U}{L}$ is the Weissenberg number.

In the above equations t is time, $\mathbf{u}$ is the velocity field, p is the pressure per unit of mass and $\mathbf{g}$ is the gravitational field. The non-dimensional parameters $Re = \rho UL/\mu$ and $Fr = U/\sqrt{gL}$ are, respectively, the Reynolds and Froude numbers. L and U are the length and the velocity scales, μ is the dynamic viscosity and ρ is the density of the fluid.

The numerical method proposed to solve Eqs. (1)–(3) is an adaptation of the GENSMAC3D method [41]. A strategy for the classification of the cells in the mesh is used to represent the moving fluid. Fig. 1(a) illustrates this classification for a two-dimensional flow (in Fig. 1(a) the empty cells are represented by blank cells). In the present work, the same cell classification is used, that is

- Empty Cell (E): Cells that do not contain fluid;
- Full Cell (F): Cells that contain fluid and do not possess any faces in contact with empty cell faces;

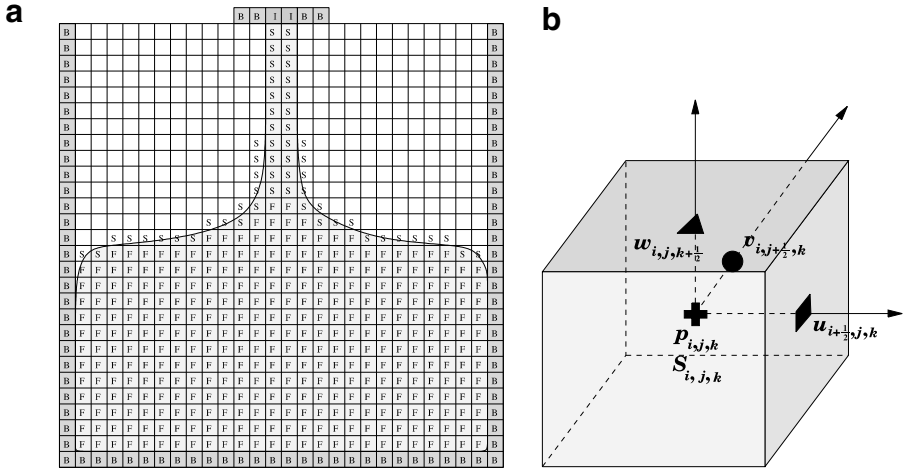

Fig. 1. Type of cells (a) and position of the variables u, v, w, p and S on the staggered grid (b).

- Surface Cell (S): Cells that contain fluid and necessarily have faces in contact with empty cell faces;
- Boundary Cell (B): Cells that define the positions of rigid boundaries;
- Inflow Cell (I): Cells that define entrance of the fluid (inflow);
- Outflow Cell (O): Cells that define exit of the fluid (outflow).

In order to solve Eqs. (1)–(3) a staggered grid is employed. A typical cell for the three-dimensional case is shown in Fig. 1(b).

2.1. Initial and boundary conditions

Eqs. (1) and (2) consist of a system of partial differential equations for the unknowns u, v, w and p. To solve this system we need to impose appropriate initial and boundary conditions. In practice, there are four types of boundaries to be considered, namely: inflows, outflows, solid walls and moving free surfaces. At inflows the velocity is known ($\mathbf{u} = \mathbf{u}_{\text{inf}}$) and at outflows homogeneous Neumann conditions ($\frac{\partial \mathbf{u}}{\partial n} = \mathbf{0}$) are specified. On solid walls, it is assumed that the fluid adheres to the surface ($\mathbf{u} = \mathbf{0}$).

On the moving free surface, it is necessary to impose conditions for the velocity and pressure. If surface tension forces are neglected, then these conditions can be summarized as

$$\mathbf{n} \cdot \boldsymbol{\sigma} \cdot \mathbf{n} = 0, \tag{4}$$

and

$$\mathbf{m1} \cdot \boldsymbol{\sigma} \cdot \mathbf{n} = 0 \quad \text{and} \quad \mathbf{m2} \cdot \boldsymbol{\sigma} \cdot \mathbf{n} = 0, \tag{5}$$

where $\boldsymbol{\sigma}$ is the stress tensor given by

$$\boldsymbol{\sigma} = -p\mathbf{I} + \alpha \frac{1}{Re}\left[(\nabla \mathbf{u}) + (\nabla \mathbf{u})^{\mathrm{T}}\right] + \beta \mathbf{S}, \tag{6}$$

where, again, $\alpha = 1$ and $\beta = 0$ for Newtonian flows and $\alpha = \lambda_2/\lambda_1$ and $\beta = 1$ for Oldroyd-B fluids.

In Eqs. (4) and (5), $\mathbf{n} = (n_1, n_2, n_3)$ represents the unit normal vector external to the surface, and $\mathbf{m1} = (m_{11}, m_{12}, m_{13})$ and $\mathbf{m2} = (m_{21}, m_{22}, m_{23})$ are the unit tangent vectors to the free surface. If we take Cartesian coordinates, then Eqs. (4), (5) can be written as (see [44])

$$\begin{aligned} p = {} & \alpha \frac{2}{Re}\left[\frac{\partial u}{\partial x}n_x^2 + \frac{\partial v}{\partial y}n_y^2 + \frac{\partial w}{\partial z}n_z^2 + \left(\frac{\partial v}{\partial x} + \frac{\partial u}{\partial y}\right)n_x n_y + \left(\frac{\partial w}{\partial x} + \frac{\partial u}{\partial z}\right)n_x n_z + \left(\frac{\partial w}{\partial y} + \frac{\partial v}{\partial z}\right)n_y n_z\right] \\ & + \beta\left[S^{xx}n_x^2 + S^{yy}n_y^2 + S^{zz}n_z^2 + 2\left(S^{xy}n_x n_y + S^{xz}n_x n_z + S^{yz}n_y n_z\right)\right], \end{aligned} \tag{7}$$

$$\begin{aligned} & 2\frac{\partial u}{\partial x}n_x m_{1x} + 2\frac{\partial zv}{\partial y}n_y m_{1y} + 2\frac{\partial w}{\partial z}n_z m_{1z} + \left(\frac{\partial v}{\partial x} + \frac{\partial u}{\partial y}\right)(m_{1x}n_y + m_{1y}n_x) + \left(\frac{\partial w}{\partial x} + \frac{\partial u}{\partial z}\right)(m_{1x}n_z + m_{1z}n_x) \\ & + \left(\frac{\partial w}{\partial y} + \frac{\partial v}{\partial z}\right)(m_{1y}n_z + m_{1z}n_y) = -Re\frac{\beta}{\alpha}\left[S^{xx}n_x m_{1x} + S^{yy}n_y m_{1y} + S^{zz}n_z m_{1z} + S^{xy}\left(m_{1x}n_y + m_{1y}n_x\right)\right. \\ & \left. + S^{xz}(m_{1x}n_z + m_{1z}n_x) + S^{yz}\left(m_{1y}n_z + m_{1z}n_x\right)\right], \end{aligned} \tag{8}$$

$$\begin{aligned} & 2\frac{\partial u}{\partial x}n_x m_{2x} + 2\frac{\partial v}{\partial y}n_y m_{2y} + 2\frac{\partial w}{\partial z}n_z m_{2z} + \left(\frac{\partial v}{\partial x} + \frac{\partial u}{\partial y}\right)(m_{2x}n_y + m_{2y}n_x) + \left(\frac{\partial w}{\partial x} + \frac{\partial u}{\partial z}\right)(m_{2x}n_z + m_{2z}n_x) \\ & + \left(\frac{\partial w}{\partial y} + \frac{\partial v}{\partial z}\right)(m_{2y}n_z + m_{2z}n_y) = -Re\frac{\beta}{\alpha}[S^{xx}n_x m_{2x} + S^{yy}n_y m_{2y} + S^{zz}n_z m_{2z} + S^{xy}\left(m_{2x}n_y + m_{2y}n_x\right) \\ & + S^{xz}(m_{2x}n_z + m_{2z}n_x) + S^{yz}\left(m_{2y}n_z + m_{2z}n_x\right)]. \end{aligned} \tag{9}$$

Eqs. (7)–(9) represent the appropriate boundary conditions at a fluid free surface (see Batchelor page 153 [4]). It is known that three-dimensional free surface flows are highly affected by the manner in which these conditions are applied. However, several authors approximate the normal stress condition (7) simply by setting $p = 0$ (e.g. [3,27,22]). This could be used only in the case of Newtonian flows possessing $Re \gg 1$. The tangential conditions have usually been ignored (see [24]).

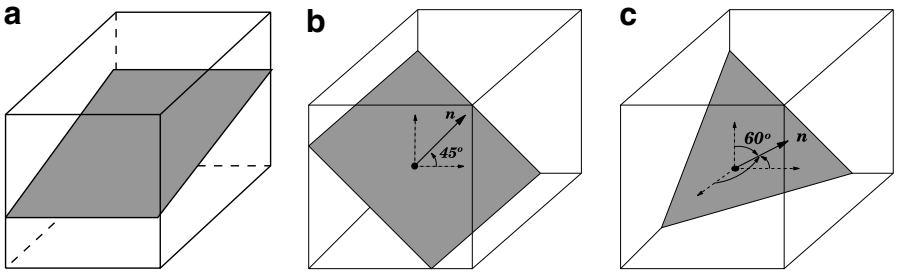

Fig. 2. Types of planar surfaces: (a) 1D-planar surface, (b) 2D-planar surface and (c) 3D-planar surface.

To apply the conditions above we follow the ideas presented in Tomé et al. [41]. It is supposed that the mesh spacing is sufficiently small that the free surface can be locally approximated by a planar surface. Following Tomé et al., three cases are considered.

(i) **1D-planar surfaces** parallel to one co-ordinate axis. These surfaces are identified by S-cells having only one face in contact with an E-cell face.
(ii) **2D-planar surfaces** are assumed to make 45° with two co-ordinate axes and are recognized by S-cells having two adjacent faces in contact with E-cell faces.
(iii) **3D-planar surfaces** are considered to be surfaces that make 60° with three co-ordinate axes and are represented by S-cells having three adjacent faces in contact with E-cell faces. Fig. 2 displays examples of 1D, 2D and 3D-planar surfaces. By using these three types of approximations for the free surface, the normal stress condition (7) is used to compute the pressure on the free surface while the tangential stress conditions, Eqs. (8) and (9), are employed to calculate the velocities at the empty cells. For details see [41].

An implicit technique involving the normal stress condition will be described in Section 3.1.

3. Numerical method

The numerical method for solving Eqs. (1) and (2) will be based on the projection method (pioneered by Chorin [9]) while the constitutive Eq. (3) is approximated by a second-order finite difference method. In summary, the solution of the momentum Eq. (1) is obtained by calculating a provisional velocity field followed by the solution of an elliptic equation to enforce mass conservation (2).

The projection methods are based on the Helmholtz decomposition (see [11]) which states that every smooth vector field can be decomposed as a sum of a gradient and a divergence-free vector field, i.e.,

$$\widetilde{\mathbf{u}} = \mathbf{u} + \nabla\phi. \tag{10}$$

Many authors (e.g. [6,16,17,34]) have proposed different versions of the projection method for confined Newtonian flow calculations and recently there have been a few papers dealing with free surface flows (see e.g. [17,32,47]). We use these ideas to solve the equations for viscoelastic free surface flows as follows:

There are several ways to solve Eqs. (1) and (2) using implicit techniques (e.g. [5,6,20,21]). However, we are interested in low Reynolds number free surface viscoelastic flows so that the convective terms are not important while the non-Newtonian stress tensor $\mathbf{S}$ is defined by an hyperbolic equation and is treated as a source term. Thus, if we use the Crank–Nicolson method for the viscous term then Eqs. (1) and (2) can be written in the form

$$\frac{\mathbf{u}^{n+1}}{\delta t} - \frac{\alpha}{2Re}\nabla^2\mathbf{u}^{n+1} = \frac{\mathbf{u}^n}{\delta t} - \nabla\cdot(\mathbf{uu})^n - \nabla p^{n+1} + \frac{\alpha}{2Re}\nabla^2\mathbf{u}^n + \beta\nabla\cdot\mathbf{S}^n + \frac{1}{Fr^2}\mathbf{g}^n, \tag{11}$$

$$\nabla\cdot\mathbf{u}^{n+1} = 0. \tag{12}$$

To uncouple the velocity and pressure fields in Eqs. (11) and (12) we apply the projection method as follows.

First, we solve Eq. (11) for a provisional velocity field $\widetilde{\mathbf{u}}$

$$\frac{\widetilde{\mathbf{u}}}{\delta t} - \frac{\alpha}{2Re}\nabla^2\widetilde{\mathbf{u}} = \frac{\mathbf{u}^n}{\delta t} - \nabla\cdot(\mathbf{u}\mathbf{u})^n - \nabla p^n + \frac{\alpha}{2Re}\nabla^2\mathbf{u}^n + \beta\nabla\cdot\mathbf{S}^n + \frac{1}{Fr^2}\mathbf{g}^n, \tag{13}$$

where the boundary conditions for $\widetilde{\mathbf{u}}$ are the same as for $\mathbf{u}^n$, and p^n represents the pressure at time $t = t_n$. Using Eq. (10), the velocity field can be decomposed as

$$\mathbf{u}^{n+1} = \widetilde{\mathbf{u}} - \nabla\phi^{n+1} = \widetilde{\mathbf{u}} - \delta t\nabla\psi^{n+1}. \tag{14}$$

Taking the divergence of Eq. (14) and imposing mass conservation for $\mathbf{u}^{n+1}$, one obtains the following Poisson equation for ψ^{n+1}

$$\nabla^2\psi^{n+1} = \frac{1}{\delta t}\nabla\cdot\widetilde{\mathbf{u}}. \tag{15}$$

This equation is solved in the fluid region and is applied at each full cell F within the mesh. The equations for ψ^{n+1} on the free surface are discussed in the next section.

To obtain an equation for the pressure, we introduce $\widetilde{\mathbf{u}}$ from Eq. (14) into Eq. (13) and then subtract it from Eq. (11) to obtain

$$p^{n+1} = p^n + \psi^{n+1} - \alpha\frac{\delta t}{2Re}\nabla^2\psi^{n+1}. \tag{16}$$

Thus, the velocity and the pressure field are obtained by solving Eqs. (13)–(16).

The non-Newtonian stress tensor $\mathbf{S}$ is calculated from the Oldroyd-B constitutive equation

$$\frac{\partial\mathbf{S}}{\partial t} = -(\mathbf{u}^{n+1}\cdot\nabla)\mathbf{S} + (\nabla\mathbf{u}^{n+1})^{\mathrm{T}}\mathbf{S} + \mathbf{S}(\nabla\mathbf{u}^{n+1}) + \frac{1}{We}\left[-\mathbf{S} + \frac{1}{Re}\left(1 - \frac{\lambda_2}{\lambda_1}\right)((\nabla\mathbf{u}^{n+1}) + (\nabla\mathbf{u}^{n+1})^{\mathrm{T}})\right]. \tag{17}$$

Eq. (17) is solved by an explicit Euler approximation.

3.1. Implicit formulation for the pressure at the free surface

Recently, Oishi et al. [28] presented a two-dimensional numerical technique using the implicit Euler method to solve the provisional velocity field together with a methodology to calculate the pressure on the free surface. The pressure was calculated by the simpler equation

$$p^{n+1} = p^n + \psi^{n+1}. \tag{18}$$

In this work we shall employ Eq. (16) to compute the pressure on the free surface using implicit techniques.

Following the ideas of [28], the equation for the pressure at the free surface (7) will be treated implicitly, whereas the tangential conditions given by Eqs. (8) and (9) will be discretized explicitly. Eq. (7), in discrete form, can then be rewritten as

$$\begin{aligned} p^{n+1} = {} & \alpha\frac{2}{Re}\left[\frac{\partial u}{\partial x}n_x^2 + \frac{\partial v}{\partial y}n_y^2 + \frac{\partial w}{\partial z}n_z^2 + \left(\frac{\partial v}{\partial x} + \frac{\partial u}{\partial y}\right)n_x n_y + \left(\frac{\partial w}{\partial x} + \frac{\partial u}{\partial z}\right)n_x n_z + \left(\frac{\partial w}{\partial y} + \frac{\partial v}{\partial z}\right)n_y n_z\right]^{n+1} \\ & + \beta\left[S^{xx}n_x^2 + S^{yy}n_y^2 + S^{zz}n_z^2 + 2(S^{xy}n_x n_y + S^{xz}n_x n_z + S^{yz}n_y n_z)\right]^n. \end{aligned} \tag{19}$$

We point out that this equation couples the velocity and the pressure and a strategy for decoupling them was essential for the algorithm to be competitively efficient. The strategy we adopted uses the equation for the corrected velocity and the pressure (see Eqs. (14) and (16)) to construct new equations for the potential ψ^{n+1} at the free surface. In previous works (e.g. [38,41,42]), the pressure was calculated explicitly using Eq. (7) so that ψ^{n+1} was set to zero on the free surface cells.

In what follows we present a derivation of the equations corresponding to each type of free surface approximation given in Section 2.1.

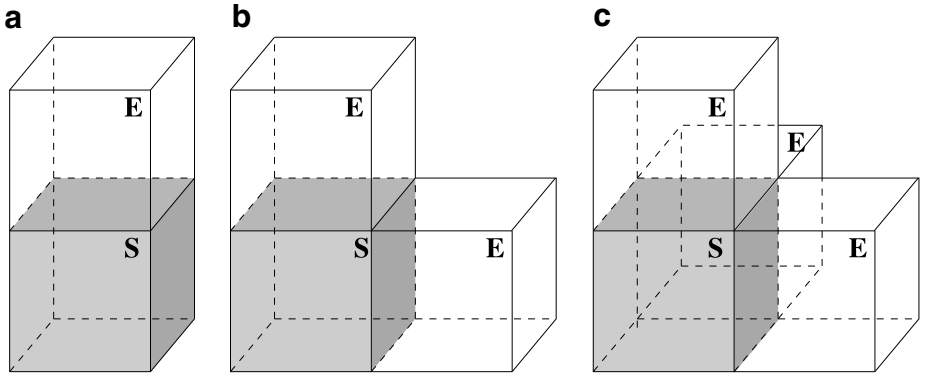

Fig. 3. (a) Normal vector is pointing in the direction of one of the co-ordinate directions, (b) normal vector is pointing in a direction making 45° with two adjacent co-ordinate axes, and (c) normal vector is pointing in a direction making 60° with two adjacent co-ordinate axes.

(i) 1D-planar surfaces: To illustrate how Eq. (19) might be employed to obtain an equation for the potential ψ^{n+1} at the free surface, let us consider the particular case of a S-cell with the $(k+\frac{1}{2})$-face in contact with an E-cell face as shown in Fig. 3a. In this case, the normal vector is $\mathbf{n} = (0,0,1)$ ($\mathbf{n} = (0,0,-1)$ results in the same equation) and Eq. (19) is reduced to

$$p^{n+1} = \alpha \frac{2}{Re}\left(\frac{\partial w^{n+1}}{\partial z}\right) + \beta (S^{zz})^n. \tag{20}$$

Now, from the mass conservation Eq. (2) discretized at time level $n+1$ we have

$$\frac{\partial w^{n+1}}{\partial z} = -\frac{\partial u^{n+1}}{\partial x} - \frac{\partial v^{n+1}}{\partial y}, \tag{21}$$

and introducing it into Eq. (20) we obtain

$$p^{n+1} = -\alpha \frac{2}{Re}\left(\frac{\partial u^{n+1}}{\partial x} + \frac{\partial v^{n+1}}{\partial y}\right) + \beta (S^{zz})^n. \tag{22}$$

Eq. (14), written in component form, yields

$$\begin{cases} u^{n+1} = \widetilde{u} - \delta t \frac{\partial \psi^{n+1}}{\partial x}, \\ v^{n+1} = \widetilde{v} - \delta t \frac{\partial \psi^{n+1}}{\partial y}, \\ w^{n+1} = \widetilde{w} - \delta t \frac{\partial \psi^{n+1}}{\partial z}, \end{cases} \tag{23}$$

so that introducing u^{n+1} and v^{n+1} into Eq. (22) we obtain

$$p^{n+1} = \alpha \frac{2}{Re}\left(-\frac{\partial \widetilde{u}}{\partial x} + \delta t \frac{\partial^2 \psi^{n+1}}{\partial x^2} - \frac{\partial \widetilde{v}}{\partial y} + \delta t \frac{\partial^2 \psi^{n+1}}{\partial y^2}\right) + \beta (S^{zz})^n. \tag{24}$$

Finally, substituting Eq. (16) into Eq. (24) and regrouping the terms we obtain the following equation for the potential ψ^{n+1}

$$\psi^{n+1} - \alpha \frac{\delta t}{2Re} \nabla^2 \psi^{n+1} - \alpha \frac{2\delta t}{Re}\left(\frac{\partial^2 \psi^{n+1}}{\partial x^2} + \frac{\partial^2 \psi^{n+1}}{\partial y^2}\right) = -\alpha \frac{2}{Re}\left(\frac{\partial \widetilde{u}}{\partial x} + \frac{\partial \widetilde{v}}{\partial y}\right) - p^n + \beta (S^{zz})^n. \tag{25}$$

The other cases of 1D-planar surfaces with $\mathbf{n} = (0, \pm 1, 0)$ and $\mathbf{n} = (\pm 1, 0, 0)$ are treated similarly.

(ii) 2D-planar surfaces: Let us consider the S-cell in Fig. 3b. For this cell we assume the normal vector is given by $\mathbf{n} = \left(\frac{\sqrt{2}}{2}, 0, \frac{\sqrt{2}}{2}\right)$ and Eq. (19) becomes

$$p^{n+1} = \frac{\alpha}{Re}\left(\frac{\partial u^{n+1}}{\partial x} + \frac{\partial w^{n+1}}{\partial z} + \frac{\partial u^{n+1}}{\partial z} + \frac{\partial w^{n+1}}{\partial x}\right) + \beta\left[\frac{1}{2}S^{xx} + \frac{1}{2}S^{zz} + S^{xz}\right]^n, \tag{26}$$

and, upon using the mass conservation equation, simplifies to

$$p^{n+1} = \frac{\alpha}{Re}\left(-\frac{\partial v^{n+1}}{\partial y} + \frac{\partial u^{n+1}}{\partial z} + \frac{\partial w^{n+1}}{\partial x}\right) + \beta\left[\frac{1}{2}S^{xx} + \frac{1}{2}S^{zz} + S^{xz}\right]^n. \tag{27}$$

Now, substituting u^{n+1}, v^{n+1} and w^{n+1} from Eq. (23) into Eq. (27) we get

$$p^{n+1} = \frac{\alpha}{Re}\left(-\frac{\partial \widetilde{v}}{\partial y} + \delta t\frac{\partial^2 \psi^{n+1}}{\partial y^2} + \frac{\partial \widetilde{u}}{\partial z} - \delta t\frac{\partial^2 \psi^{n+1}}{\partial x \partial z} + \frac{\partial \widetilde{w}}{\partial x} - \delta t\frac{\partial^2 \psi^{n+1}}{\partial x \partial z}\right) + \beta\left[\frac{1}{2}S^{xx} + \frac{1}{2}S^{zz} + S^{xz}\right]^n. \tag{28}$$

The equation for ψ^{n+1} is obtained by substituting Eq. (16) into Eq. (28) and after regrouping the terms we obtain

$$\psi^{n+1} - \alpha\frac{\delta t}{2Re}\nabla^2\psi^{n+1} - \alpha\frac{\delta t}{Re}\left(\frac{\partial^2 \psi^{n+1}}{\partial y^2} - 2\frac{\partial^2 \psi^{n+1}}{\partial x \partial z}\right) = -\frac{\alpha}{Re}\left(\frac{\partial \widetilde{v}}{\partial y} - \frac{\partial \widetilde{u}}{\partial z} - \frac{\partial \widetilde{w}}{\partial x}\right) - p^n + \beta\left[\frac{1}{2}S^{xx} + \frac{1}{2}S^{zz} + S^{xz}\right]^n. \tag{29}$$

We have presented the equations for a S-cell with the faces $(i+\frac{1}{2})$ and $(k+\frac{1}{2})$ in contact with E-cell faces. The corresponding equations for the other configurations of S-cells having two adjacent faces contiguous with E-cell faces are obtained in a similar manner.

(**iii**) **3D-planar surfaces**: In total there are 8 possible configurations of these surfaces. We will present the equations for a S-cell with the faces $(i+\frac{1}{2})$, $(j+\frac{1}{2})$ and $(k+\frac{1}{2})$ in contact with the faces of E-cells (see Fig. 3c). For this case, we take $\mathbf{n} = \left(\frac{\sqrt{3}}{3}, \frac{\sqrt{3}}{3}, \frac{\sqrt{3}}{3}\right)$ and Eq. (19) becomes

$$p^{n+1} = \alpha\frac{2}{3Re}\left(\frac{\partial u^{n+1}}{\partial y} + \frac{\partial v^{n+1}}{\partial x} + \frac{\partial u^{n+1}}{\partial z} + \frac{\partial w^{n+1}}{\partial x} + \frac{\partial v^{n+1}}{\partial z} + \frac{\partial w^{n+1}}{\partial y}\right) + \beta\frac{1}{3}[S^{xx} + S^{yy} + S^{zz} + 2(S^{xy} + S^{xz} + S^{yz})]^n, \tag{30}$$

and, upon introducing u^{n+1}, v^{n+1} and w^{n+1} from Eq. (23), we obtain

$$p^{n+1} = \alpha\frac{2}{3Re}\left(\frac{\partial \widetilde{u}}{\partial y} + \frac{\partial \widetilde{u}}{\partial z} + \frac{\partial \widetilde{v}}{\partial x} + \frac{\partial \widetilde{v}}{\partial z} + \frac{\partial \widetilde{w}}{\partial x} + \frac{\partial \widetilde{w}}{\partial y} - 2\delta t\left[\frac{\partial^2 \psi^{n+1}}{\partial y \partial x} + \frac{\partial^2 \psi^{n+1}}{\partial z \partial x} + \frac{\partial^2 \psi^{n+1}}{\partial z \partial y}\right]\right) + \beta\frac{1}{3}[S^{xx} + S^{yy} + S^{zz} + 2(S^{xy} + S^{xz} + S^{yz})]^n. \tag{31}$$

The final equation for ψ^{n+1} is obtained by introducing Eq. (16) into Eq. (31) and, after some simplifications, the following is obtained:

$$\psi^{n+1} - \alpha\frac{\delta t}{2Re}\nabla^2\psi^{n+1} + \alpha\frac{4\delta t}{3Re}\left[\frac{\partial^2 \psi^{n+1}}{\partial y \partial x} + \frac{\partial^2 \psi^{n+1}}{\partial z \partial x} + \frac{\partial^2 \psi^{n+1}}{\partial z \partial y}\right] = \alpha\frac{2}{3Re}\left(\frac{\partial \widetilde{u}}{\partial y} + \frac{\partial \widetilde{u}}{\partial z} + \frac{\partial \widetilde{v}}{\partial x} + \frac{\partial \widetilde{v}}{\partial z} + \frac{\partial \widetilde{w}}{\partial x} + \frac{\partial \widetilde{w}}{\partial y}\right) + \beta\frac{1}{3}[S^{xx} + S^{yy} + S^{zz} + 2(S^{xy} + S^{xz} + S^{yz})]^n - p^n. \tag{32}$$

The equations for ψ^{n+1} corresponding to the other configurations of 3D-planar surfaces are carried out in a similar way.

We observe that when solving these equations for surface cells, the values of ψ^{n+1} on empty cells will be involved in which case $\psi^{n+1} = 0$.

3.2. Algorithm

It is supposed that at time t_0, the solenoidal-velocity field $\mathbf{u}(x, y, z, t_0)$ is known and suitable boundary conditions for the velocity and pressure are given. The updated velocity field $\mathbf{u}(x, y, z, t)$, the pressure field $p(x, y, z, t)$ and the non-Newtonian stress tensor $\mathbf{S}(x, y, z, t)$ at time $t = t_0 + \delta t$ are calculated by the following sequence of the steps:

STEP 1: Calculate the intermediate velocity field $\widetilde{\mathbf{u}}(x,y,z,t)$ from Eq. (13) implicitly using a Crank–Nicolson discretization.

STEP 2: Solve the Poisson Eq. (15) together with the equations derived for the potential function ψ^{n+1} at the free surface (see Section 3.1). The appropriate boundary conditions for these equations are $\psi^{n+1}=0$ on outflows while the homogeneous Neumann condition is used for fixed boundaries and inflows. The resulting linear system for ψ^{n+1} is sparse and non-symmetric: we therefore employ the bi-conjugated gradient method with pre-conditioning to solve this linear system. The corresponding finite difference equations will be given in the next section.

STEP 3: Compute the final velocity field from (14).

STEP 4: Compute the pressure from (16).

STEP 5: Calculate the stress tensor **S** from Eq. (17). This equation is solved by explicit finite differences and the details of the equations involved can be found in Tomé et al. [44].

STEP 6: Update the positions of the marker particles by solving

$$\dot{\mathbf{x}} = \mathbf{u}^{n+1}, \tag{33}$$

by the explicit Euler's method.

3.3. Finite difference equations

We present only the finite difference approximations corresponding to the equations of **STEP 1**, **STEP 2** and **STEP 4** of the computational algorithm outlined in the previous sub-section. The corresponding finite difference equations for **STEP 3**, **STEP 5** and **STEP 6** can be found in the references [41,44].

The momentum equation, Eq. (13), is approximated as follows: the time derivative and the viscous terms are approximated by the Crank–Nicolson method while the pressure gradient and the divergence of the non-Newtonian stress tensor **S** are discretized using central differences. The convective terms are calculated by the high order upwind scheme CUBISTA of Alves et al. [1]. Details of the finite difference equations for the CUBISTA method can be found in [14]. For instance, the x-component of the momentum equation is approximated by the following difference equation

$$\begin{aligned}
&\left[1+\left(\frac{\delta t\alpha}{Re}\right)\left(\frac{1}{\delta x^2}+\frac{1}{\delta y^2}+\frac{1}{\delta z^2}\right)\right]\widetilde{u}_{i+\frac{1}{2},j,k}-\left(\frac{\delta t\alpha}{2Re\delta x^2}\right)\left(\widetilde{u}_{i+\frac{3}{2},j,k}+\widetilde{u}_{i-\frac{1}{2},j,k}\right)\\
&\quad-\left(\frac{\delta t\alpha}{2Re\delta y^2}\right)\left(\widetilde{u}_{i+\frac{1}{2},j+1,k}+\widetilde{u}_{i+\frac{1}{2},j-1,k}\right)-\left(\frac{\delta t\alpha}{2Re\delta z^2}\right)\left(\widetilde{u}_{i+\frac{1}{2},j,k+1}+\widetilde{u}_{i+\frac{1}{2},j,k-1}\right)\\
&\quad=u^n_{i+\frac{1}{2},j,k}+\delta t\left[-(\mathcal{C}(uu)+\mathcal{C}(vu)+\mathcal{C}(wu))^n-\left(\frac{p_{i+1,j,k}-p_{i,j,k}}{\delta x}\right)^n\right.\\
&\qquad+\frac{\alpha}{2Re}\left(\frac{u_{i-\frac{1}{2},j,k}-2u_{i+\frac{1}{2},j,k}+u_{i+\frac{3}{2},j,k}}{\delta x^2}+\frac{u_{i+\frac{1}{2},j-1,k}-2u_{i+\frac{1}{2},j,k}+u_{i+\frac{1}{2},j+1,k}}{\delta y^2}+\frac{u_{i+\frac{1}{2},j,k-1}-2u_{i+\frac{1}{2},j,k}+u_{i+\frac{1}{2},j,k+1}}{\delta z^2}\right)^n\\
&\qquad\left.+\beta\left(\frac{S^{xx}_{i+1,j,k}-S^{xx}_{i,j,k}}{\delta x}+\frac{S^{yx}_{i+\frac{1}{2},j+\frac{1}{2},k}-S^{yx}_{i+\frac{1}{2},j-\frac{1}{2},k}}{\delta y}+\frac{S^{zx}_{i+\frac{1}{2},j,k+\frac{1}{2}}-S^{zx}_{i+\frac{1}{2},j,k-\frac{1}{2}}}{\delta z}\right)^n+\frac{1}{Fr^2}g_x\right],
\end{aligned} \tag{34}$$

where the convective terms $\mathcal{C}(uu)$, $\mathcal{C}(vu)$ and $\mathcal{C}(wu)$ are approximated by the CUBISTA method. Terms like $S^{yx}_{i+\frac{1}{2},j+\frac{1}{2},k}$ are obtained by averaging its nearest neighbours, for instance,

$$S^{yx}_{i+\frac{1}{2},j+\frac{1}{2},k}=\frac{S^{yx}_{i,j,k}+S^{yx}_{i+1,j,k}+S^{yx}_{i,j+1,k}+S^{yx}_{i+1,j+1,k}}{4}.$$

The y- and z-components of the momentum equations are obtained in the same way. Therefore, the calculation of the provisional velocity field $\widetilde{\mathbf{u}}$ leads to the solution of three symmetric linear systems which are solved by the conjugate gradient method. The implementation of the conjugate gradient solver follows the ideas presented by Tomé and McKee [40].

3.3.1. Calculation of the potential function ψ^{n+1}

The Poisson Eq. (15) is discretized by the following second-order difference equation

$$\frac{\psi^{n+1}_{i+1,j,k}-2\psi^{n+1}_{i,j,k}+\psi^{n+1}_{i-1,j,k}}{\delta x^2}+\frac{\psi^{n+1}_{i,j+1,k}-2\psi^{n+1}_{i,j,k}+\psi^{n+1}_{i,j-1,k}}{\delta y^2}+\frac{\psi^{n+1}_{i,j,k+1}-2\psi^{n+1}_{i,j,k}+\psi^{n+1}_{i,j,k-1}}{\delta z^2}$$
$$=\delta t^{-1}\left(\frac{\widetilde{u}_{i+\frac{1}{2},j,k}-\widetilde{u}_{i-\frac{1}{2},j,k}}{\delta x}+\frac{\widetilde{v}_{i,j+\frac{1}{2},k}-\widetilde{v}_{i,j-\frac{1}{2},k}}{\delta y}+\frac{\widetilde{w}_{i,j,k+\frac{1}{2}}-\widetilde{w}_{i,j,k-\frac{1}{2}}}{\delta z}\right). \tag{35}$$

Eq. (35) is applied at each full cell in the domain. The calculation of $\psi^{n+1}_{i,j,k}$ at surface cells is carried out following the ideas detailed in Section 3.1 with appropriate approximations for each type of surface, i.e. **1D**, **2D** or **3D**-planar surfaces. For instance, if we consider a S-cell having only the top face in contact with an E-cell as shown in Fig. 4 then we assume that the free surface is a **1D**-planar surface parallel to the x- and y-axes and take $\mathbf{n}=(0,0,1)$. In this case, $\psi^{n+1}_{i,j,k}$ is given by Eq. (25) which becomes

$$\left[1+\left(\frac{\alpha\delta t}{Re}\right)\left(\frac{5}{\delta x^2}+\frac{5}{\delta y^2}+\frac{1}{\delta z^2}\right)\right]\psi^{n+1}_{i,j,k}-\left(\frac{5\alpha\delta t}{2Re\delta x^2}\right)\left[\psi^{n+1}_{i+1,j,k}+\psi^{n+1}_{i-1,j,k}\right]-\left(\frac{5\alpha\delta t}{2Re\delta y^2}\right)\left[\psi^{n+1}_{i,j+1,k}+\psi^{n+1}_{i,j-1,k}\right]$$
$$-\left(\frac{\alpha\delta t}{2Re\delta z^2}\right)\psi^{n+1}_{i,j,k-1}=\frac{-2\alpha}{Re}\left(\frac{\widetilde{u}_{i+\frac{1}{2},j,k}-\widetilde{u}_{i-\frac{1}{2},j,k}}{\delta x}+\frac{\widetilde{v}_{i,j+\frac{1}{2},k}-\widetilde{v}_{i,j-\frac{1}{2},k}}{\delta y}\right)-p^{n}_{i,j,k}+\beta(S^{zz})^{n}_{i,j,k}. \tag{36}$$

In Eq. (36) the potential $\psi^{n+1}_{i,j,k+1}$ does not appear because it is assumed that it is zero in empty cells. The finite difference equations for the other configurations of **1D**-planar surfaces are obtained in a similar manner.

For surface cells having two adjacent faces in contact with empty cell faces the potential $\psi^{n+1}_{i,j,k}$ is computed by using the equations derived for **2D**-planar surfaces. For instance if a S-cell has the $(i+\frac{1}{2})$ and $(k+\frac{1}{2})$-faces contiguous with E-cell faces then $\psi^{n+1}_{i,j,k}$ is calculated from Eq. (29) applied at the centre of the surface cell. The second derivatives are approximated by second-order differences while the derivatives $\frac{\partial^2\psi^{n+1}}{\partial x\partial z}$, $\frac{\partial\widetilde{u}}{\partial z}$ and $\frac{\partial\widetilde{w}}{\partial x}$ are replaced, respectively, by the first-order approximations

$$\left.\frac{\partial^2\psi^{n+1}}{\partial x\partial z}\right|_{i,j,k}=\frac{(\psi^{n+1}_{i,j,k}-\psi^{n+1}_{i-1,j,k}-\psi^{n+1}_{i,j,k-1}+\psi^{n+1}_{i-1,j,k-1})}{\delta x\delta z}, \tag{37}$$

$$\left.\frac{\partial\widetilde{u}}{\partial z}\right|_{i,j,k}=\frac{\widetilde{u}_{i,j,k}-\widetilde{u}_{i,j,k-1}}{\delta z},\quad \left.\frac{\partial\widetilde{w}}{\partial x}\right|_{i,j,k}=\frac{\widetilde{w}_{i,j,k}-\widetilde{w}_{i-1,j,k}}{\delta x}. \tag{38}$$

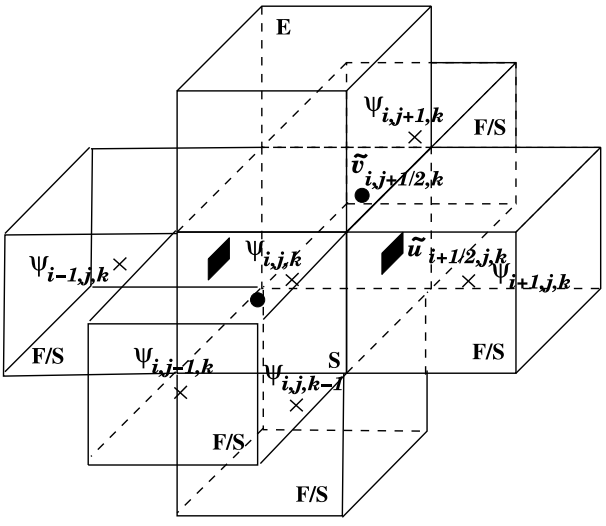

Fig. 4. Surface cell with only the top face in contact with an empty cell face.

In Eq. (38), the values of the tilde-velocities at the centre of the cells are approximated by the values in the inner cells, namely,

$$\widetilde{u}_{i,j,k} \approx \widetilde{u}_{i-\frac{1}{2},j,k}, \widetilde{u}_{i,j,k-1} \approx \widetilde{u}_{i-\frac{1}{2},j,k-1}, \quad \widetilde{w}_{i,j,k} \approx \widetilde{w}_{i,j,k-\frac{1}{2}}, \widetilde{w}_{i-1,j,k} \approx \widetilde{w}_{i-1,j,k-\frac{1}{2}}.$$

Thus, by introducing these approximations into Eq. (29) and regrouping the terms, we obtain the following difference equation

$$\begin{aligned}
&\left[1+\left(\frac{\alpha\delta t}{Re}\right)\left(\frac{1}{\delta x^2}+\frac{3}{\delta y^2}+\frac{1}{\delta z^2}+\frac{2}{\delta x\delta z}\right)\right]\psi^{n+1}_{i,j,k}-\left(\frac{\alpha\delta t}{Re}\right)\left(\frac{1}{2\delta x^2}+\frac{2}{\delta x\delta z}\right)\psi^{n+1}_{i-1,j,k}\\
&-\left(\frac{3\alpha\delta t}{2Re\delta y^2}\right)\left[\psi^{n+1}_{i,j+1,k}+\psi^{n+1}_{i,j-1,k}\right]-\left(\frac{\alpha\delta t}{Re}\right)\left(\frac{1}{2\delta z^2}+\frac{2}{\delta x\delta z}\right)\psi^{n+1}_{i,j,k-1}+\left(\frac{2\alpha\delta t}{Re\delta x\delta z}\right)\psi^{n+1}_{i-1,j,k-1}\\
&=\frac{-\alpha}{Re}\left(\frac{\widetilde{v}_{i,j+\frac{1}{2},k}-\widetilde{v}_{i,j-\frac{1}{2},k}}{\delta y}-\left.\frac{\partial\widetilde{u}}{\partial z}\right|_{i,j,k}-\left.\frac{\partial\widetilde{w}}{\partial x}\right|_{i,j,k}\right)-p^{n}_{i,j,k}+\beta\left[\frac{1}{2}S^{xx}_{i,j,k}+\frac{1}{2}S^{zz}_{i,j,k}+S^{xz}_{i,j,k}\right]^{n}.
\end{aligned} \tag{39}$$

Again, we point out that the potentials $\psi^{n+1}_{i+1,j,k}$ and $\psi^{n+1}_{i,j,k+1}$ do not appear in the equation above because they lie in empty cells where they are assumed to be zero. The equations for $\psi^{n+1}_{i,j,k}$ at surface cells with two empty cell neighbours, but different configurations, are treated similarly.

For surface cells having three adjacent faces in contact with empty cell faces, the finite difference equations for the potential can be obtained similarly. For instance, if we consider a S-cell with the faces $(i+\frac{1}{2})$, $(j+\frac{1}{2})$ and $(k+\frac{1}{2})$ in contact with E-cells then the potential $\psi^{n+1}_{i,j,k}$ is calculated from Eq. (32). To approximate this equation by finite differences we proceed as in the case of surface cells with two adjacent faces in contact with empty cell faces (e.g. see Eq. (39)). The cross derivatives are first-order approximated (see Eq. (37)) and the second-order derivatives of ψ^{n+1} are approximated by central differences. Thus, Eq. (32) is approximated by the following difference equation

$$\begin{aligned}
&\left[1+\left(\frac{\alpha\delta t}{Re}\right)\left(\frac{1}{\delta x^2}+\frac{1}{\delta y^2}+\frac{1}{\delta z^2}+\frac{4}{3\delta x\delta y}+\frac{4}{3\delta x\delta z}+\frac{4}{3\delta y\delta z}\right)\right]\psi^{n+1}_{i,j,k}\\
&-\left(\frac{\alpha\delta t}{Re}\right)\left(\frac{1}{2\delta x^2}+\frac{4}{3\delta x\delta y}+\frac{4}{3\delta x\delta z}\right)\psi^{n+1}_{i-1,j,k}-\left(\frac{\alpha\delta t}{Re}\right)\left(\frac{1}{2\delta y^2}+\frac{4}{3\delta x\delta y}+\frac{4}{3\delta y\delta z}\right)\psi^{n+1}_{i,j-1,k}\\
&-\left(\frac{\alpha\delta t}{Re}\right)\left(\frac{1}{2\delta z^2}+\frac{4}{3\delta x\delta z}+\frac{4}{3\delta y\delta z}\right)\psi^{n+1}_{i,j,k-1}+\left(\frac{\alpha\delta t}{Re}\right)\frac{4}{3\delta x\delta y}\psi^{n+1}_{i-1,j-1,k}+\left(\frac{\alpha\delta t}{Re}\right)\frac{4}{3\delta x\delta z}\psi^{n+1}_{i-1,j,k-1}\\
&+\left(\frac{\alpha\delta t}{Re}\right)\frac{4}{3\delta y\delta z}\psi^{n+1}_{i,j-1,k-1}=\frac{2\alpha}{3Re}\left(\left.\frac{\partial\widetilde{u}}{\partial y}\right|_{i,j,k}+\left.\frac{\partial\widetilde{u}}{\partial z}\right|_{i,j,k}+\left.\frac{\partial\widetilde{v}}{\partial x}\right|_{i,j,k}+\left.\frac{\partial\widetilde{v}}{\partial z}\right|_{i,j,k}+\left.\frac{\partial\widetilde{w}}{\partial x}\right|_{i,j,k}+\left.\frac{\partial\widetilde{w}}{\partial y}\right|_{i,j,k}\right)-p^{n}_{i,j,k}\\
&+\beta\frac{1}{3}\left[S^{xx}_{i,j,k}+S^{yy}_{i,j,k}+S^{zz}_{i,j,k}+2\left(S^{xy}_{i,j,k}+S^{xz}_{i,j,k}+S^{yz}_{i,j,k}\right)\right]^{n}.
\end{aligned} \tag{40}$$

The other cases of surface cells having three adjacent cells with empty cell faces are dealt with similarly.

The potential function ψ^{n+1} is then calculated by solving a sparse non-symmetric linear system composed of the equations from the discrete Poisson Eq. (35) together with the finite difference equations obtained for the surface cells (e.g. (36), (39), (40)). This linear system is efficiently solved by the preconditioned bi-conjugate gradient method with diagonal scaling.

After the potential function $\psi^{n+1}_{i,j,k}$ has been calculated for each full and surface cell, the pressure is obtained explicitly by approximating Eq. (16) at the centre of these cells by the following difference equation

$$p^{n+1}_{i,j,k}=p^{n}_{i,j,k}+\psi^{n+1}_{i,j,k}-\alpha\frac{\delta t}{2Re}\left(\frac{\psi^{n+1}_{i+1,j,k}-2\psi^{n+1}_{i,j,k}+\psi^{n+1}_{i-1,j,k}}{\delta x^2}+\frac{\psi^{n+1}_{i,j+1,k}-2\psi^{n+1}_{i,j,k}+\psi^{n+1}_{i,j-1,k}}{\delta y^2}+\frac{\psi^{n+1}_{i,j,k+1}-2\psi^{n+1}_{i,j,k}+\psi^{n+1}_{i,j,k-1}}{\delta z^2}\right). \tag{41}$$

3.4. Time step calculation

If the momentum equations were solved explicitly then this would lead to the following time step restrictions:

$$\delta t < \delta t_{\mathrm{CFL}} = \max\left\{\frac{\delta x}{|u|}, \frac{\delta y}{|v|}, \frac{\delta z}{|w|}\right\}, \tag{42}$$

$$\delta t < \delta t_{\mathrm{visc}} = \frac{Re}{2}\frac{\delta x^2 \delta y^2 \delta z^2}{\delta x^2\delta y^2 + \delta x^2 \delta z^2 + \delta y^2 \delta z^2}. \tag{43}$$

Since we are employing the Crank–Nicolson we might expect the viscous time step to be unrestricted or, at least, have a less restricted stability condition. Oishi et al. [28] found in practice that the latter was the case. To gain some insight as to why this is so, Oishi et al. [29] studied the model problem of the Crank–Nicolson approximation of the one-dimensional heat equation on a staggered grid with explicit boundary conditions. They showed rigorously that the Crank–Nicolson was stable provided $r = \delta t/\delta x^2 < 2$. However, for free surface flows no analysis has yet been provided so that the time step for the implicit method will be calculated based on a relaxation of the restriction (43) as follows.

Following Tomé and McKee [40], the time step selected would be given by

$$\delta t = \mathrm{FACT} * \min\{\mathrm{FACT1} * \delta t_{\mathrm{CFL}}, \mathrm{FACT2} * \delta t_{\mathrm{visc}}\}, \tag{44}$$

where $\mathrm{FACT}, \mathrm{FACT1}, \mathrm{FACT2} > 0$. The factors FACT, FACT1, FACT2 appear as a conservative measure because the correct values of the velocities satisfying mass conservation are not known at this stage. The automatic time step selection procedure follows that outlined in Tomé et al. [41].

So far, Freeflow3D has performed explicit calculations and typical values of the constants in (44) have been 0.3 for the constant FACT and 0.5 for the constants FACT1, FACT2. However, if $Re < 1$ the relevant restriction on the time step is δt_{visc} which depends on the mesh spacing and on the Reynolds number only. Thus, if the Reynolds number is very small, which is often predictable for viscoelastic flows, the time step can be too small to employ explicit calculations in any reasonable time. However, two-dimensional calculations with the implicit method (see Oishi et al. [28]) have shown that the restriction (43) can be improved by making $\mathrm{FACT2} > 1$ so that a much larger time step can be employed when computing low Reynolds number free surface flows.

In the next section we simulate extrudate swell of Oldroyd-B fluids and jet buckling of Newtonian fluids for very small Reynolds numbers. Validation results are also presented.

4. Numerical simulation of low *Re* free surface flows

The implicit technique described in the previous sections was implemented into the Freeflow3D code (see Castelo et al. [7]) to simulate unsteady three-dimensional low Reynolds number free surface flows of Newtonian and Oldroyd-B fluids. It was used to simulate the flow of an Oldroyd-B fluid in a tube and the numerical results were compared with the analytic solution. Time-dependent extrudate swell and jet buckling for very small Reynolds numbers were also simulated. The results presented in this section were obtained on the computer: Sun Fire AMD Athlon(tm) 64/Opteron(tm), 2193 MHz, 24 Gb of RAM memory, 4 Dual core processors, under Operating System Solaris.

4.1. Validation results

To validate the numerical technique presented in this paper we simulated the flow of an Oldroyd-B fluid in a tube. We considered a tube of radius R and length $5R$ (see Fig. 5) and imposed a steady state parabolic flow at the tube entrance given by

$$w(x,y) = 2U\left[R^2 - x^2 - y^2\right], \qquad u = v = 0. \tag{45}$$

In this case, it can be shown that the analytic solutions for the components of the non-Newtonian stress tensor $\mathbf{S}$ are given by

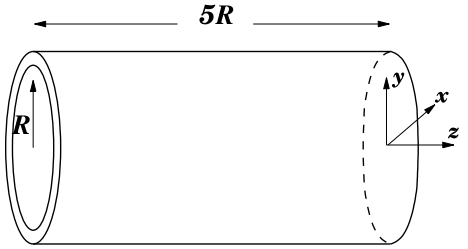

Fig. 5. Numerical simulation of the flow of an Oldroyd-B fluid in a tube: 3D case.

$$\begin{cases} S^{xy} = 0, \qquad S^{xz} = \frac{1}{Re}\left(1 - \frac{\lambda_2}{\lambda_1}\right)\frac{\partial w}{\partial x}, \quad S^{yz} = \frac{1}{Re}\left(1 - \frac{\lambda_2}{\lambda_1}\right)\frac{\partial w}{\partial y}, \\ S^{xx} = S^{yy} = 0, \qquad S^{zz} = 2\frac{We}{Re}\left(1 - \frac{\lambda_2}{\lambda_1}\right)\left[\left(\frac{\partial w}{\partial x}\right)^2 + \left(\frac{\partial w}{\partial y}\right)^2\right]. \end{cases} \tag{46}$$

The following input data were employed: $R = 1$ m, gravity was neglected, $\mu = 10$ Pa s, $\rho = 1$ kg m^{-3}, $\lambda_1 = 1$ s,$\lambda_2 = 0.5$ s. The scaling parameters were $L = R$, $U = 1$ m s^{-1}. Thus, $Re = 0.1$ and $We = 1$. To analyse the convergence of the method we employed mesh refinement and used four embedded uniform meshes defined by: M0 – $12 \times 12 \times 30$ cells ($\delta x_{M0} = 0.1667$ m), M1 – $16 \times 16 \times 40$ cells ($\delta x_{M1} = 0.1250$ m), M2 – $22 \times 22 \times 55$ cells ($\delta x_{M2} = 0.0909$ m) and M3 – $28 \times 28 \times 70$ cells ($\delta x_{M3} = 0.071428$ m).

We ran the Freeflow-3D code with the above data. We started with an empty tube and injected fluid at the tube entrance until the tube was full and the steady state had been attained.

Since $Re = 0.1$, δt was calculated using restriction δt_{visc} (43). The constants used in these simulations were chosen to be FACT = 0.5 and FACT2 = 5.0 (FACT1 was set to 0.5) for meshes M0, M1 and M2. In this case, we had time step sizes of 1.15742×10^{-3} s for mesh M0, 6.51000×10^{-4} s for mesh M1. The simulation using mesh M2 did not converge with FACT = 0.5 and therefore it was restarted with FACT = 0.1 so that the time step employed in this run was $\delta t = 6.68800 \times 10^{-5}$ s. For mesh M3 we used FACT = 0.1 which gave $\delta t = 4.25170 \times 10^{-5}$ s. In order to assess the efficiency of the implicit technique we also simulated the tube flow on mesh M0 using the explicit technique of Tomé et al. [44]. In this simulation, the time step size was calculated using Eq. (44) with FACT = 0.2 and FACT2 = 0.5 resulting in a time step size of 4.62963×10^{-5} s. To compare the accuracy of both techniques, we considered the cross section of the tube at $z = 2.5R$ and computed the relative l_2-norm of the errors

$$E(\Gamma) = \sqrt{\frac{\sum_{ij} (\Gamma_{\text{exact}} - \Gamma_{\text{numerical}})^2}{\sum_{ij} (\Gamma_{\text{exact}})^2}},$$

where Γ denotes the variables w, S^{zz}, S^{xz} or S^{yz}.

Table 1 displays the CPU time for the explicit and implicit methods, together with the relative l_2-norm of the errors using mesh M0. From Table 1 we can observe that the implicit technique is capable of employing a time step 25 times larger than that used for the explicit method and consequently the CPU time was significantly reduced demonstrating the relative efficiency of the implicit method. Moreover, we can observe in Table 1 that the errors obtained in calculating the velocity by the implicit method were of the same order as the errors given by the explicit method.

Table 1
Comparison of the performance of the explicit and the implicit techniques on mesh M0

Method	δt size	CPU time	$E(w)$	$E(S^{zz})$
Explicit	4.62963×10^{-5}	155 h 58 min	5.2198×10^{-3}	2.0589×10^{-2}
Implicit	1.15741×10^{-3}	4 h 54 min	5.2197×10^{-3}	2.0589×10^{-2}

The errors $E(S^{xz})$ and $E(S^{yz})$ were about the same for both techniques and for this reason are not shown.

Table 2
Errors obtained on meshes **M1**, **M2** and **M3**

	$E(w)$	$E(S^{zz})$	$E(S^{xz})$	$E(S^{yz})$
M1	2.6455×10^{-3}	9.4005×10^{-3}	4.8908×10^{-3}	4.8692×10^{-3}
M2	1.3845×10^{-3}	6.9864×10^{-3}	3.8249×10^{-3}	3.7656×10^{-3}
M3	8.5889×10^{-4}	3.9572×10^{-3}	2.0880×10^{-3}	2.0223×10^{-3}

Time steps used: 6.5100×10^{-4} s (**M1**), 6.6880×10^{-5} s (**M2**) and 4.2517×10^{-5} s (**M3**).

To analyse the convergence of the implicit technique we present, in Table 2, the errors obtained in calculating the velocity w using the three meshes. Additionally, Table 2 also shows the errors in the computation of the non-Newtonian stress tensor $\mathbf{S}$. We observe that the errors decreased with the mesh refinement demonstrating the convergence of this implicit technique for low Reynolds number flows.

We used the results of Table 2 and computed estimates of the order of convergence (N_i) of the implicit technique for solving the velocity field. We used the formula

$$N_i = \frac{\log\left(\frac{E(w)_{M_{i+1}}}{E(w)_{M_i}}\right)}{\log\left(\frac{\delta x_{M_{i+1}}}{\delta x_{M_i}}\right)}, \quad i = 1, 2 \tag{47}$$

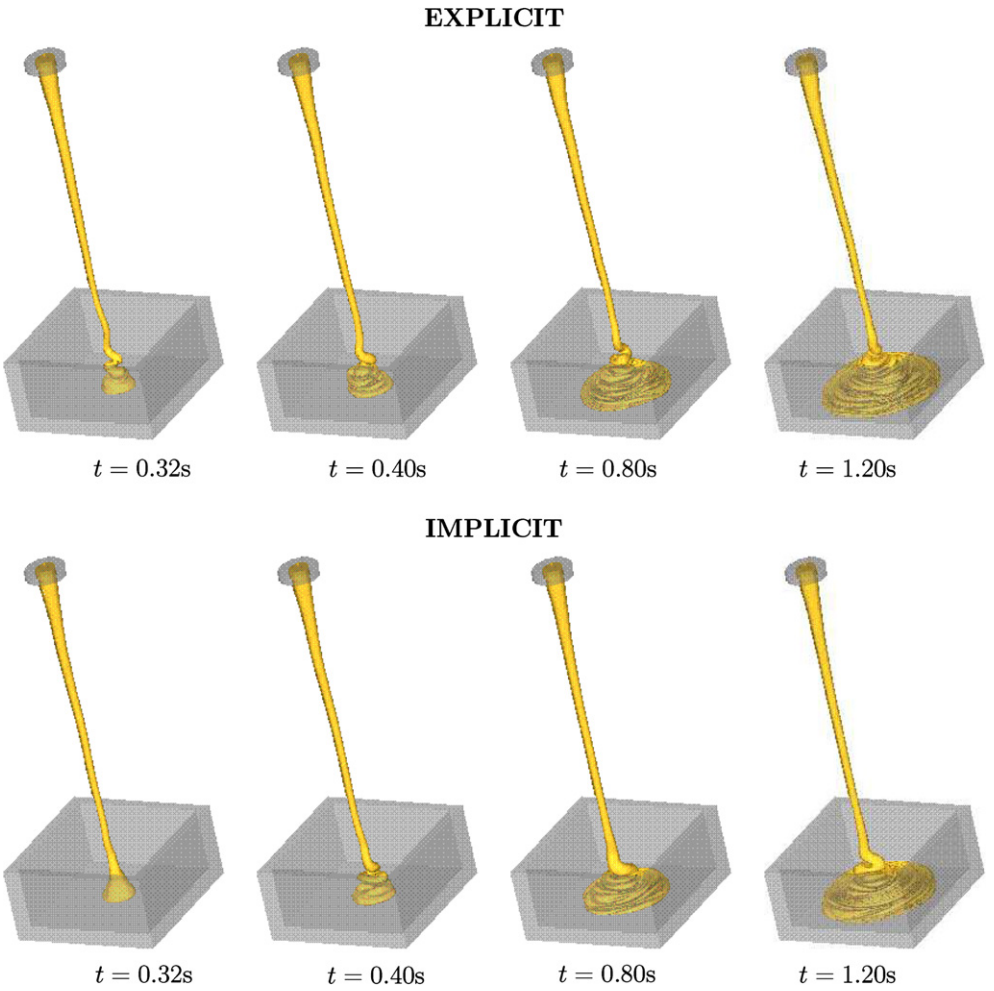

Fig. 6. Numerical simulation of jet buckling using explicit and implicit techniques. Flow visualization at selected times ($Re = 0.274$ and $Fr = 0.478$).

and obtained $N_1 = 2.03$ and $N_2 = 1.98$. These results are in agreement with the Crank–Nicolson method which is a second-order scheme.

To provide additional validation, the implicit technique was applied to simulate the jet buckling phenomenon (e.g. see [10,35–37,41]) of a very viscous fluid. We considered a low Reynolds number Newtonian axisymmetric jet flowing into an empty box which buckles (due to the high viscosity) when it reaches the box floor. This problem was simulated using both the explicit and implicit techniques. The input data used in these simulations were:

- Box size: 4 cm × 4 cm × 2 cm; inlet diameter (D): 6 mm; height of the inlet to the bottom of the box (H): 11 cm,
- Fluid specification: $\mu = 3.5$ Pa s, $\rho = 1380$ kg m^{-3},
- At the inlet we imposed a Poiseuille profile given by Eq. (45) with a mean velocity $U = 0.116$ ms^{-1}. Gravity was assumed to be acting downwards with $g = 9.81$ ms^{-2}.
- A mesh size of (60 × 60 × 110) cells was used ($\delta x = \delta y = \delta z = 1$ mm). The time step size for the explicit calculation employed FACT = 0.1 and FACT2 = 0.5 while the implicit method used FACT = 1 and FACT2 = 5. Thus, the implicit technique employed a time step 100 times larger than the time step used in the explicit simulation.

The non-dimensional parameters were U and D so that the non-dimensional numbers used in these simulations were $Re = 0.274$ and $Fr = 0.478$. We point out that Cruickshank and Munson [10] performed a series of experiments on this problem and showed that a 3D-jet will buckle if both conditions $Re < 1.2$ and $H/D > 7.2$ were satisfied. In our case, we have $Re = 0.274 < 1.2$ and $H/D = 18.33 > 7.2$ so that we would expect to observe jet buckling.

The Freeflow3D code ran this problem using the implicit and explicit approach until $t = 1.20$ s and the results are displayed in Fig. 6 at selected times. We can see in Fig. 6 that both techniques displayed the jet buckling phenomenon. Moreover, we can observe that the results obtained using the implicit technique are similar to the results displayed by the explicit method. These results, therefore provide a qualitative verification of the implementation of the implicit technique into the Freeflow3D code. In order to demonstrate the robustness and efficiency of the implicit technique we let Freeflow3D code to run this problem further on until time 2.80 s (see Fig. 7). We can see in Fig. 7 that from time $t = 1.60$ s the fluid jet reached the lateral walls of the box and continues to fill the entire box.

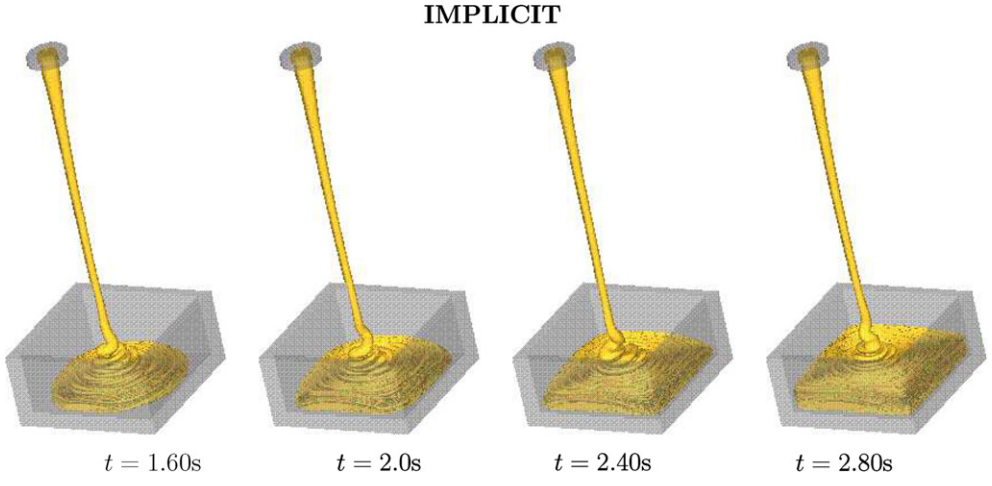

Fig. 7. Numerical simulation of jet buckling using the implicit technique. Flow visualization at selected times ($Re = 0.274$ and $Fr = 0.478$).

4.2. Numerical simulation of the unsteady extrudate swell

The extrudate swell phenomenon is generally associated with viscoelastic fluids (for Newtonian fluids the swell is not so pronounced) encountered in extrusion processes. In this problem a jet flows inside a tube of diameter D and at the tube exit the jet is ejected into the air where, due to the normal stress differences, its diameter is increased to $D_{\max}$. The extrudate swell is usually associated with low Reynolds number flows and it has been studied by many researchers: both experimental and numerical results can be found in the literature (see for instance, Liang et al. [23], Tanner [39], Tomé et al. [43]).

To demonstrate that the implicit technique presented in this paper can deal with low Reynolds free surface flows of highly viscoelastic fluids we simulated the extrudate swell of an Oldroyd-B fluid at increasing Weissenberg numbers. We considered a circular tube with length $5R$ described in the previous section (see Fig. 5) and specified an outflow boundary condition at a distance of $5R$ from the tube exit. At the tube entrance we imposed the fully developed solutions given by Eqs. (45) and (46). We used a mesh of $(16 \times 16 \times 80)$-cells ($\delta x = \delta y = \delta z = 0.625$ mm) and the constants for the time step calculation were selected to be $\mathrm{FACT} = 0.5, \mathrm{FACT2} = 5$ (see Eq. (44)). We employed the data: $R = 5$ mm, the gravity force was in the z-direction with $g = 9.81\ \mathrm{ms}^{-2}$, $\mu = 25$ Pa s, $\rho = 1000\ \mathrm{kg\,m}^{-3}, \lambda_1 = 0.01$ s. The scaling parameters were $L = R, U = 0.5\ \mathrm{ms}^{-1}$ resulting in $Re = 0.1$ and $We = 1$. To demonstrate that the implicit technique can cope with viscoelasticity we simulated the extrudate swell for three values of the effective Weissenberg number, $We_{\mathrm{effect}} = (1 - \lambda_2/\lambda_1)We$. We set $\lambda_2 = 0.008$ s, 0.005 s, 0.002 s so that we had $We_{\mathrm{effect}} = 0.2, 0.5, 0.8$, respectively. Freeflow3D then simulated the extrudate swell for these values of We_{effect}. Initially the fluid entered the empty tube, filled it and then a fluid jet was extruded into the atmosphere where eventually it reached the outflow boundary. These simulations were performed until $t = 0.45$ s for each case. The results are shown in Fig. 8 which displays the fluid flow configuration at different times. At time $t = 0.10$ s the jets are exiting the tube and the computed velocity field with the three different values of We_{effect} are similar. However, at time $t = 0.20$ s the differences between the three simulations are more noticeable. We can observe that the jet with $We_{\mathrm{effect}} = 0.8$ already displays a large swell while the jets with $We_{\mathrm{effect}} = 0.5$ and $We_{\mathrm{effect}} = 0.2$ have only started to display swelling. At time $t = 0.30$ s, we can observe the effect of gravity pulling the jets towards the outflow; indeed, the jet with $We_{\mathrm{effect}} = 0.2$ has already entered the outflow boundary. The last row of Fig. 8 presents the results obtained at time $t = 0.45$ s for the three simulations and we can clearly observe the effect of gravity on the jets. Large variations in the results were not observed between times $t = 0.4$ s and $t = 0.45$ s so that it can be assumed that steady state has been reached at that time. The final swelling ratios $S_r = D_{\max}/D$ obtained were 42.04% for $We_{\mathrm{effect}} = 0.2$, 65.15% for $We_{\mathrm{effect}} = 0.5$ and 76.47% for $We_{\mathrm{effect}} = 0.8$. To further demonstrate the applicability of the implicit technique for solving the extrudate swell for low Reynolds numbers, we simulated the extrudate swell for $Re = 0.05$ using the same input data used for $Re = 0.1$. The results obtained (see Fig. 9) are similar to those for $Re = 0.1$; the only difference between the two cases was the larger swelling ratios obtained for $Re = 0.05$. The final swelling ratios obtained were 45.71% for $We_{\mathrm{effect}} = 0.2$, 73.91% for $We_{\mathrm{effect}} = 0.5$ and 85.71% for $We_{\mathrm{effect}} = 0.8$. These results are qualitatively in agreement with those found in the literature (e.g. [23]).

4.3. Numerical simulation of jet buckling

To further demonstrate that the implicit method can cope with free surface flows of very viscous fluids we simulated jet buckling of Newtonian fluids for very low Reynolds numbers. We considered a thin axisymmetric jet, with diameter $D = 4$ mm, flowing into an empty square box at a prescribed velocity. An inlet (inflow boundary) was positioned at a height of 6 cm above the box floor from which an axisymmetric jet was issued at a velocity of $U = 0.5\ \mathrm{ms}^{-1}$. The density of the fluid was $\rho = 1000\ \mathrm{kg\,m}^{-3}$ and the viscosity was assigned the values of $\mu = 4, 20, 40, 200$ Pa s so that the Reynolds number ($Re = \rho UD/\mu$) took the values of $Re = 0.5, 0.1, 0.05, 0.01$, respectively. A mesh size of $(80 \times 80 \times 120)$-cells was employed. In these simulations $H/D = 15 > 7.2$ and $Re < 1$ so that we expected jet buckling to occur in all of these simulations. A total of four simulations were performed and the results are displayed in Figs. 10–13. The results corresponding to $Re = 0.5$ (see Fig. 10) and $Re = 0.1$ (see Fig. 11) show that the jets start to buckle earlier than for the jets with $Re = 0.05$ and $Re = 0.01$. The familiar effect known as "jet coiling" was observed; this has been well docu-

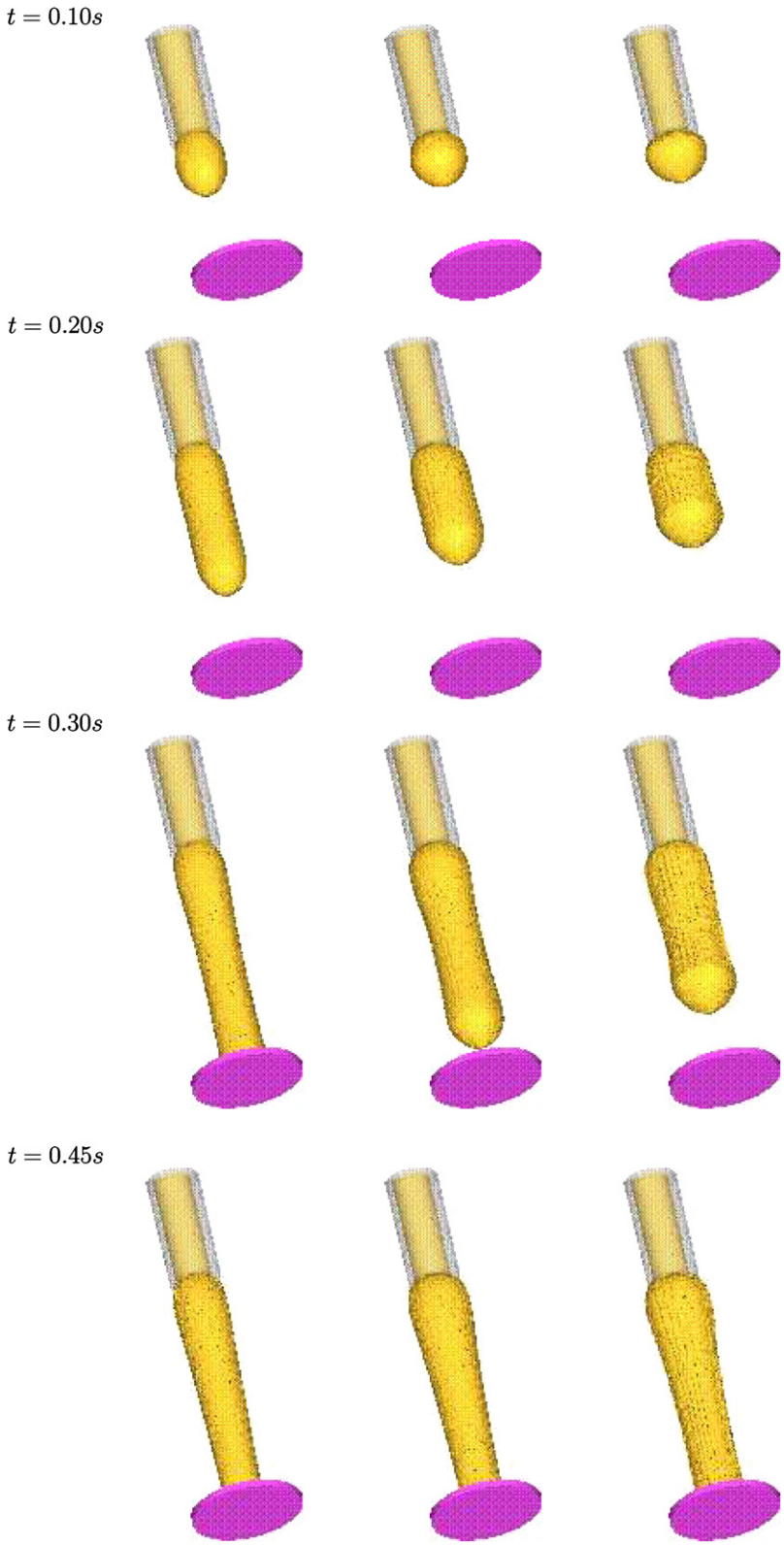

Fig. 8. Numerical simulation of the unsteady extrudate swell problem for various values of We_{effect}: 0.2 (first column); 0.5 (second column); 0.8 (third column). Fluid flow visualization at selected times. $Re = 0.1$.

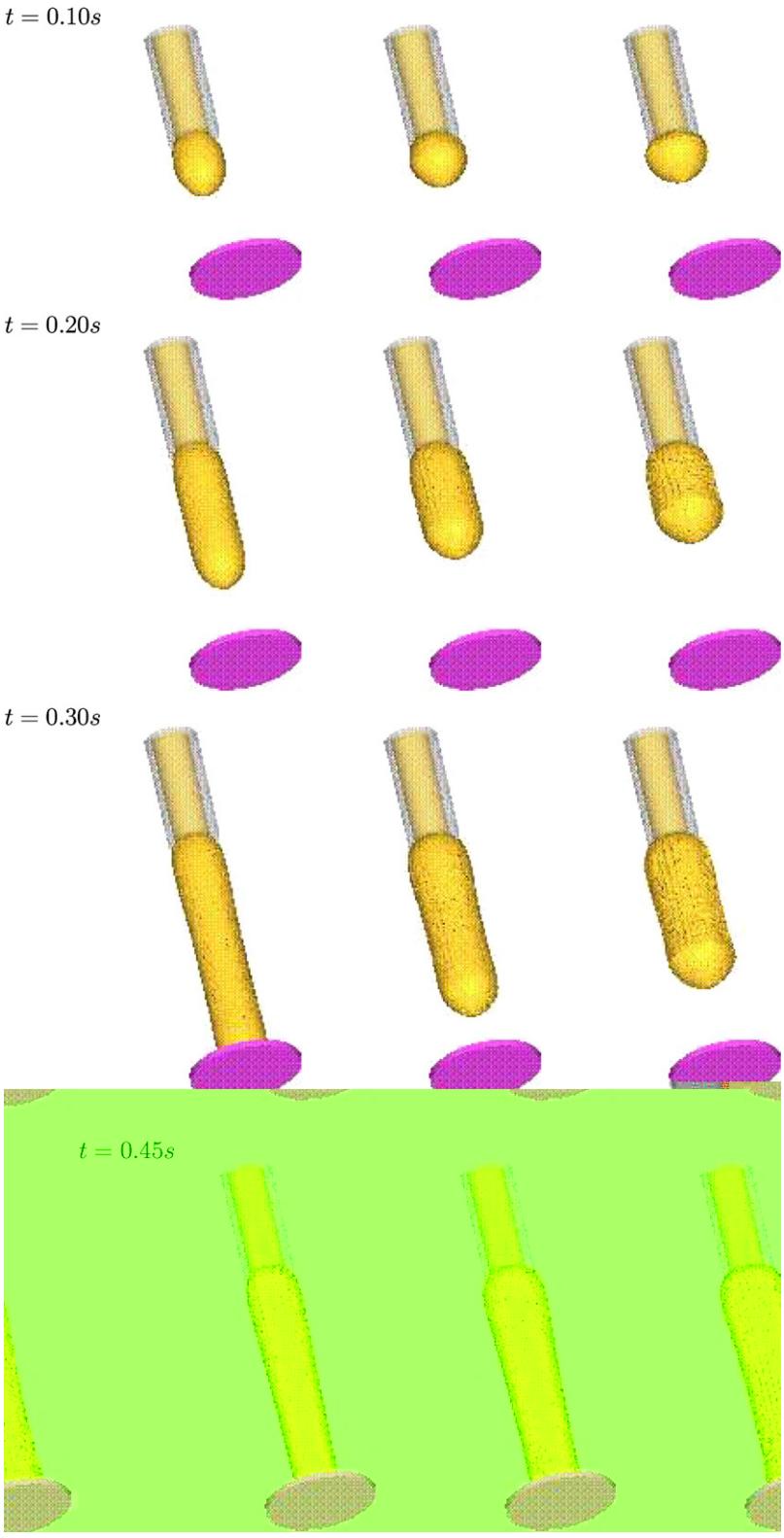

Fig. 9. Numerical simulation of the unsteady extrudate swell problem for various values of We_{effect}: 0.2 (first column); 0.5 (second column); 0.8 (third column). Fluid flow visualization at selected times. $Re = 0.05$.

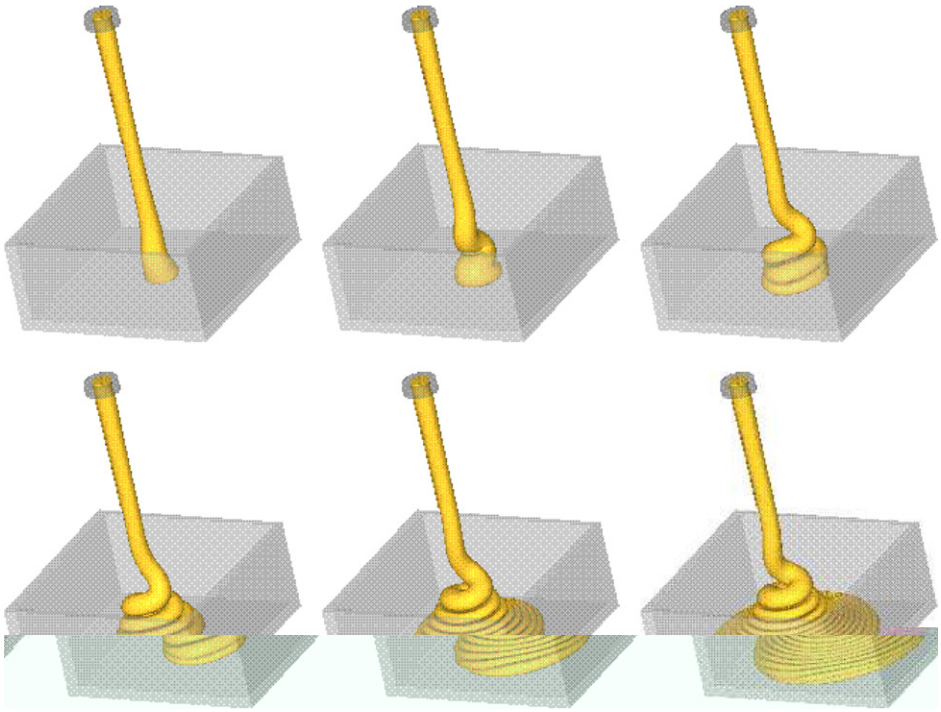

Fig. 10. Numerical simulation of jet buckling using the implicit technique ($Re = 0.5$). Fluid flow visualization at times $t = 0.14$ s, 0.20 s, 0.30 s, 0.40 s, 0.70 s and 1.0 s.

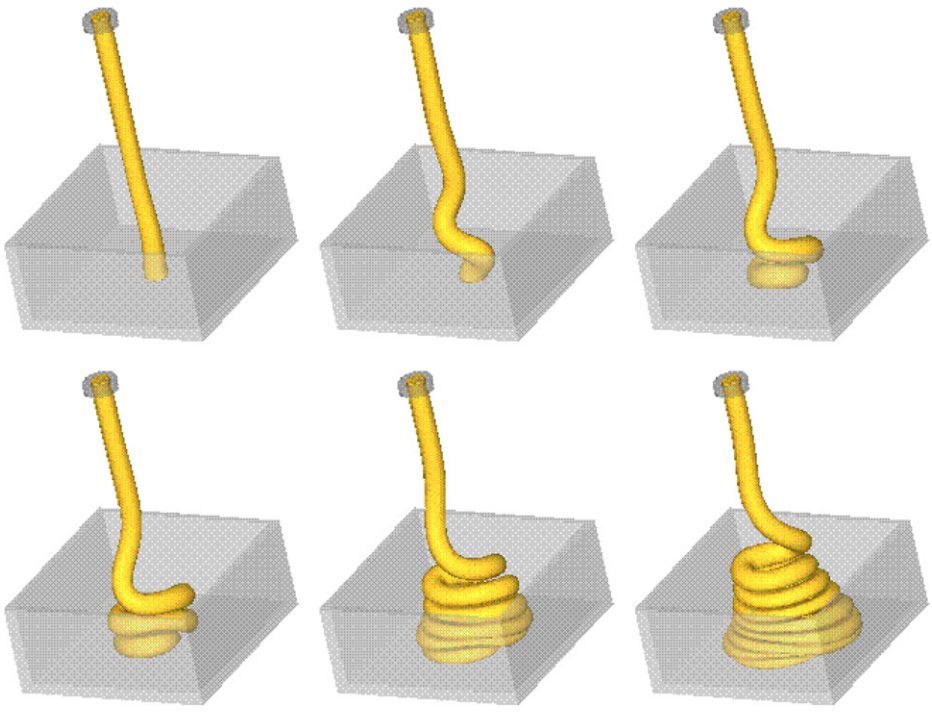

Fig. 11. Numerical simulation of jet buckling using the implicit technique ($Re = 0.1$). Fluid flow visualization at times $t = 0.14$ s, 0.20 s, 0.30 s, 0.40 s, 0.70 s and 1.0 s.

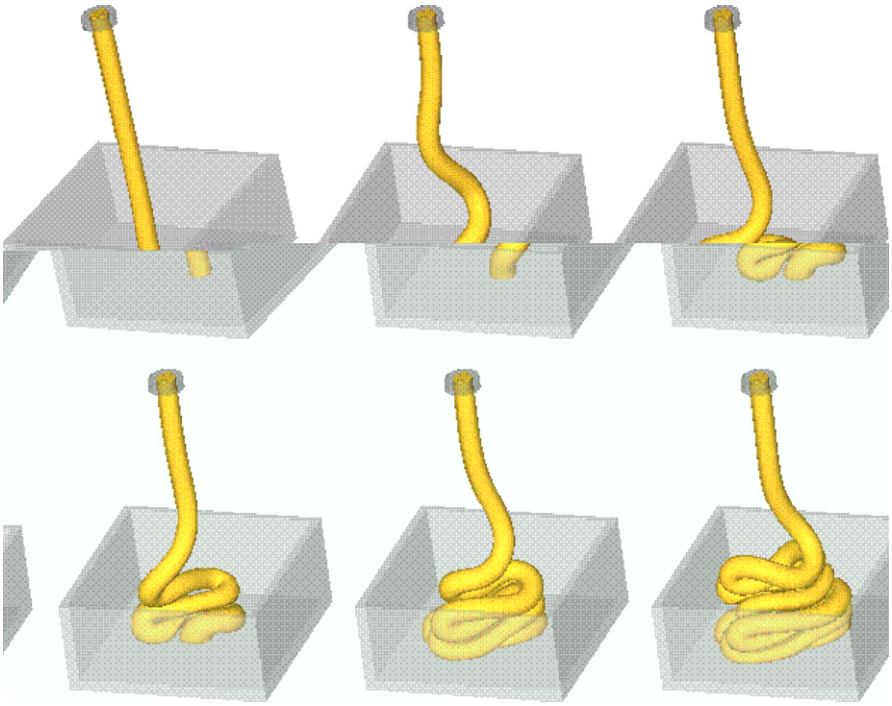

Fig. 12. Numerical simulation of jet buckling using the implicit technique ($Re = 0.05$). Fluid flow visualization at times $t = 0.14$ s, 0.20 s, 0.30 s, 0.40 s, 0.70 s and 1.0 s.

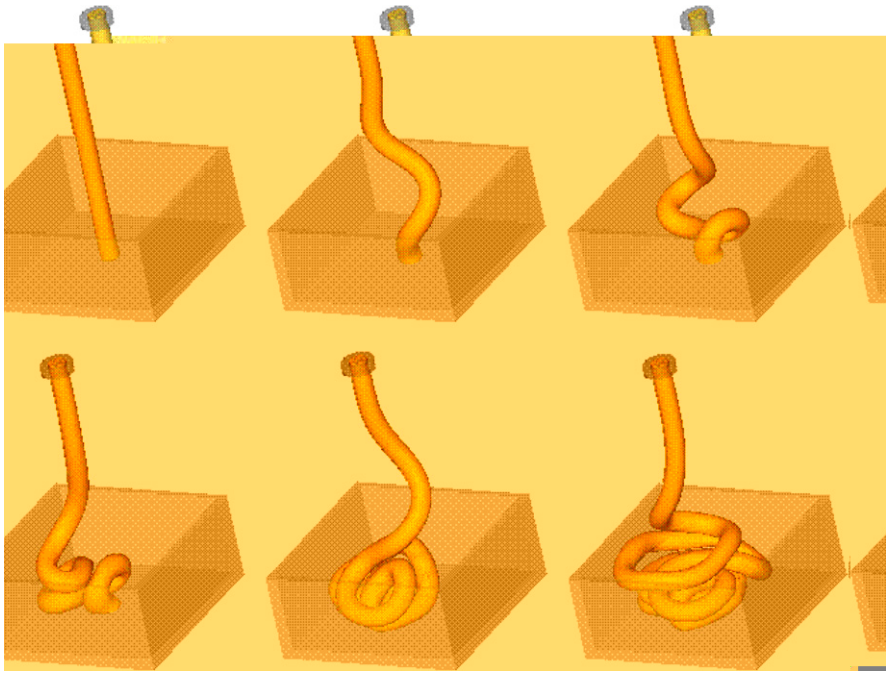

Fig. 13. Numerical simulation of jet buckling using the implicit technique ($Re = 0.01$). Fluid flow visualization at times $t = 0.14$ s, 0.20 s, 0.30 s, 0.40 s, 0.70 s and 1.0 s.

mented in the literature (see [10,35,36,41]). However, as the Reynolds number is decreased (see Figs. 12, 13) the jets first become thicker and eventually they fold in an apparently chaotic manner. This effect has been encountered experimentally and reported by Ribe and co-workers [36,37].

5. Concluding remarks

This paper has dealt with the development of an implicit technique for solving three-dimensional free surface flows of Newtonian and Oldroyd-B fluids. The momentum equations were solved by the Crank–Nicolson technique and an implicit method for treating the pressure on the free surface was developed so that the pressure and the velocity fields could be decoupled. The Oldroyd-B constitutive equation has been solved using an explicit finite difference technique developed by Tomé et al. [44]. The numerical method described in Section 3 has been implemented into the Freeflow3D code. The code then simulated the flow inside a 3D tube using three meshes and compared the numerical results with known analytic solutions. The numerical computations displayed good agreement with the respective analytic solutions and mesh refinement indicated the convergence of this implicit technique. Further validation was provided by comparing the results of the simulation of jet buckling with the results obtained with the original explicit approach. The implicit technique was then used to solve two dynamic three-dimensional free surface flow problems: extrudate swell of highly viscoelastic fluids and jet buckling of Newtonian fluids were solved. Both problems had very low Reynolds numbers. It should perhaps be pointed out that for low Reynolds number Newtonian flows one should not employ this approach: one should directly solve the creeping flow equations. However, this work is really aimed at viscoelastic flows where the "Reynolds number" may be small in one part of the spatial domain or at points in time. Mould filling would be a typical example and in these cases the use of this implicit discretization leads to two orders of magnitude improvement in the computing time.

Acknowledgements

The authors would like to acknowledge the financial support of FAPESP (Fundação de Amparo a pesquisa do Estado de São Paulo) (Grants No. 03/12612 − 9 and 04/16064 − 9), CNPq (Conselho Nacional de Desenvolvimento Científico e Tecnológico) (Grant No. 300106/2005-0) and CAPES (Coordenação de Aperfeiçoamento de Pessoal de Nível Superior) (Grant No. 136/05-CAPES/GRICES). The second author has been supported by CNPq under grants 474040/2003 − 8, 523141/94 and CAPES pos-doc Grant No. 0121/07 − 0.

This work was performed during the sabbatical leave of Prof. M. Tomé with Prof. F.T. Pinho at CEFT/FEUP (Transport Phenomena Research Center/Faculty of Engineering of University of Porto, Portugal).

References

[1] M. Alves, P. Oliveira, F. Pinho, A convergent and universally bounded interpolation scheme for the treatment of advection, Int. J. Numer. Methods Fluids 41 (2003) 47–75.
[2] A.A. Amsden, F.H. Harlow, A simplified MAC technique for incompressible fluid flow calculations, J. Comput. Phys. 6 (1970) 332–335.
[3] V. Armenio, An improved MAC method (SIMAC) for unsteady high-Reynolds free surface flows, Int. J. Numer. Methods Fluids 24 (1997) 185–214.
[4] G.K. Batchelor, An Introduction to Fluid Dynamics, Cambridge, 1970.
[5] J.B. Bell, P. Colella, H.M. Glaz, A second-order projection method for the incompressible Navier–Stokes equations, J. Comput. Phys. 85 (1989) 257–283.
[6] D.L. Brown, R. Cortez, M.L. Minion, Accurate projection methods for the incompressible Navier–Stokes equations, J. Comput. Phys. 168 (2001) 464–499.
[7] A.F. Castelo, M.F. Tomé, M.L. Cesar, J.A. Cuminato, S. McKee, Freeflow: an integrated simulation system for three-dimensional free surface flows, Comput. Vis. Sci. 2 (2000) 199–210.
[8] R.K.C. Chan, R.L. Street, A computer study of finite-amplitude water waves, J. Comput. Phys. 6 (1970) 68–94.
[9] A.J. Chorin, Numerical solution of the Navier–Stokes equations, J. Comput. Phys. 2 (1968) 745–762.
[10] J.O. Cruickshank, B.R. Munson, Viscous fluid buckling of plane and axisymmetric jets, J. Fluid Mech. 113 (1981) 221–239.
[11] F.M. Denaro, On the applications of the Helmholtz–Hodge decomposition in projection methods for incompressible flows with general boundary conditions, Int. J. Numer. Methods Fluids 43 (2003) 43–69.

[12] R.P. Fedkiw, T. Aslam, B. Merriman, S. Osher, A non-oscillatory Eulerian approach to interfaces in multi-material flows (the ghost fluid method), J. Comput. Phys. 152 (1999) 457–492.
[13] V.G. Ferreira, C.M. Oishi, F.A. Kurokawa, M.A. Kaibara, J.A. Cuminato, A. Castelo A, M.F. Tomé, N. Mangiavacchi, S. McKee, A combination of implicit and adaptative upwind tools for the numerical solution of incompressible free surface flows, Commun. Numer. Methods Eng. 23 (2007) 419–445.
[14] V.G. Ferreira, A.C. Brandi, F.A. Kurokawa, P. Seleghim, A. Castelo, J.A. Cuminato, Incompressible turbulent flow simulation using K–E model and upwind schemes, Math. Probl. Eng. 2007 (2007) 1–26.
[15] M. Golafashani, A simple numerical technique for transient creep flows with free surfaces, Int. J. Numer. Methods Fluids 8 (1988) 897–912.
[16] J.L. Guermond, J. Shen, A new class of truly consistent splitting schemes for incompressible flows, J. Comput. Phys. 192 (2003) 262–276.
[17] J.L. Guermond, P. Minev, J. Shen, An overview of projection methods for incompressible flows, Comp. Methods Appl. Mech. Eng. 195 (2006) 6011–6045.
[18] F.H. Harlow, J.E. Welch, Numerical calculation of time-dependent viscous incompressible flow of fluid with free surface, Phys. Fluids 8 (1965) 2182–2189.
[19] C.W. Hirt, A.A. Amsden, J.L. Cook, An arbitrary Lagrangian–Eulerian computing method for all flow speeds, J. Comput. Phys. 14 (1974) 227–253.
[20] H. Johnston, J.G. Liu, Accurate, stable and efficient Navier–Stokes solvers based on explicit treatment of the pressure term, J. Comput. Phys. 199 (2004) 221–259.
[21] W. Kress, P. Lotstedt, Time step restrictions using semi-explicit methods for incompressible Navier–Stokes equations, Comp. Methods Appl. Mech. Eng. 195 (2006) 4433–4447.
[22] C. Lemos, High-order schemes for free surface flows with arbitrary configurations, Int. J. Numer. Methods Fluids 23 (1996) 545–566.
[23] Y. Liang, A. Ozetkin, S. Neti, Dynamics of viscoelastic jets of polymeric liquid extrudate, J. Non-Newtonian Fluid Mech. 81 (1999) 105–132.
[24] H. Miyata, A. Masuko, Finite-difference simulation of non-linear waves generated by ships of arbitrary three-dimensional configuration, J. Comput. Phys. 60 (1985) 391–436.
[25] H. Miyata, Finite-difference simulation of breaking waves, J. Comput. Phys. 65 (1986) 179–214.
[26] D.Q. Nguyen, R.P. Fedkiw, M. Kang, A boundary condition capturing method for incompressible flame discontinuities, J. Comput. Phys. 172 (2001) 71–98.
[27] B.D. Nichols, C.W. Hirt, R.S. Hotchkiss, SOLA-VOF: a solution algorithm for transient fluid flow with multiple free boundaries, Los Alamos Scientific Laboratory Report LA8355, Los Alamos, New Mexico, 1980.
[28] C.M. Oishi, J.A. Cuminato, V.G. Ferreira, M.F. Tomé, A. Castelo, N. Mangiavacchi, S. McKee, A stable semi-implicit method for free surface flows, Trans. ASME J. Appl. Mech. 73 (2006) 940–947.
[29] C.M. Oishi, J.A. Cuminato, J.Y. Yuan, S. McKee, Stability of numerical schemes on staggered grids, Numer. Linear Algebra Appl., accepted for publication.
[30] C.M. Oishi, V.G. Ferreira, J.A. Cuminato, A semi-implicit finite difference method for 3D incompressible free surface flow simulation, in: Proceedings of the II LNCC Meeting on Computational Modelling, Petrópolis, Brazil, 2006.
[31] C.M. Oishi, V.G. Ferreira, J.A. Cuminato, N. Mangiavacchi, A second-order projection method for free surface flows, in: Proceedings of the XXVII Iberian Latin American Congress on Computational Methods in Engineering, Belém, Brazil, 2006.
[32] B. Perot, R. Nallapati, A moving unstructured staggered mesh method for the simulation of incompressible free surface flows, J. Comput. Phys. 184 (2003) 192–214.
[33] W.E. Pracht, A numerical method for calculating transient creep flows, J. Comput. Phys. 7 (1971) 46–60.
[34] J.H. Pyo, J. Shen, Normal mode analysis of second-order projection methods for incompressible flows, Discrete Cont. Dyn. B 5 (2005) 817–840.
[35] N.M. Ribe, Periodic folding of viscous jets, Phys. Rev. E 68 (2003), pp. Art. No. 036305 Part 2.
[36] N.M. Ribe, Coiling of viscous jets, Proceedings of the Royal Society of London Series A – Mathematical Physical and Engineering Sciences 460 (2004) 3223–3239.
[37] N.M. Ribe, H.E. Huppert, M.A. Hallworth, M. Habibie, D. Bonn, Multiple coexisting states of liquid rope coiling, J. Fluid Mech. 555 (2006) 275–297.
[38] F.S. de Sousa, N. Mangiavacchi, L.G. Nonato, A. Castelo, M.F. Tomé, V.G. Ferreira, J.A. Cuminato, S. McKee, A front-tracking/front-capturing method for the simulation of 3D multi-fluid flows with free surfaces, J. Comput. Phys. 198 (2004) 469–499.
[39] R.I. Tanner, A theory of die-swell, J. Polym. Sci. 8 (1970) 2067–2078.
[40] M.F. Tomé, S. McKee, GENSMAC: a computational marker-and-cell method for free surface flows in general domains, J. Comput. Phys. 110 (1994) 171–186.
[41] M.F. Tomé, A. Castelo, J.A. Cuminato, N. Mangiavacchi, S. McKee, GENSMAC3D: a numerical method for solving unsteady three-dimensional free surface flows, Int. J. Numer. Methods Fluids 37 (2001) 747–796.
[42] M.F. Tomé, L. Grossi, A. Castelo, J.A. Cuminato, N. Mangiavacchi, V.G. Ferreira, F.S. de Sousa, S. McKee, A numerical method for solving three-dimensional generalized Newtonian free surface flows, J. Non-Newtonian Fluid Mech. 123 (2004) 85–103.
[43] M.F. Tomé, L. Grossi, A. Castelo, J.A. Cuminato, S. McKee, K. Walters, Die-swell, splashing drop and a numerical technique for solving the Oldroyd-B model for axisymmetric free surface flows, J. Non-Newtonian Fluid Mech. 141 (2007) 148–166.
[44] M.F. Tomé, A. Castelo, V.G. Ferreira, S. McKee, A finite difference technique for solving the Oldroyd-B model for 3D-unsteady free surface flows, J. Non-Newtonian Fluid Mech., accepted for publication.

[45] S. Vincent, J.-P. Caltagirone, Efficient solving method for unsteady incompressible interfacial flow problems, Int. J. Numer. Methods Fluids 30 (1999) 795–811.
[46] S. Vincent, J.-P. Caltagirone, A one-cell local multigrid method for solving unsteady incompressible multiphase flows, J. Comput. Phys. 163 (2000) 172–215.
[47] B. Yang, A. Prosperetti, A second-order boundary-fitted projection method for free surface flow computations, J. Comput. Phys. 231 (2006) 574–590.